Comparison of remote sensing based approaches for mapping bathymetry of shallow, clear water rivers

E. Kasvi [a,*], J. Salmela [a], E. Lotsari [a,b], T. Kumpula [b], S.N. Lane [c]

[a] University of Turku, Department of Geography and Geology, FI-20014, Finland
[b] University of Eastern Finland, Department of Geographical and Historical Studies, FI-80101 Joensuu, Finland
[c] University of Lausanne, Institute of Earth Surface Dynamics, CH-1015 Lausanne, Switzerland

ARTICLE INFO

ABSTRACT

Shallow rivers provide important habitat for various aquatic and terrestrial species. The bathymetry of such environments is, however, difficult to measure as devices and approaches have been traditionally developed mainly for deeper waters. This study addresses the mapping of shallow water bathymetry with high spatial resolution and accuracy by comparing three remote sensing (RS) approaches: one based on echo sounding (active RS) and two on photogrammetry (passive RS): bathymetric Structure from Motion (SfM) and optical modelling. The tests were conducted on a 500 m long and ~30 m wide reach of sand-bedded meandering river: (1) during a rising spring flood (Q = 10–15 m^3/s) with medium turbidity and high water color and; (2) during autumn low discharge (Q = 4 m^3/s) with low turbidity and color. Each method was used to create bathymetric models. The models were compared with high precision field measurements with a mean point spacing of 0.86 m. Echo sounding provided the most accurate (ME~−0.02 m) and precise (SDE = ± 0.08 m) bathymetric models despite the high degree of interpolation needed. However, the echo sounding-based models were spatially restricted to areas deeper than 0.2 m and no small scale bathymetric variability was captured. The quality of the bathymetric SfM was highly sensitive to flow turbidity and color and therefore depth. However, bathymetric SfM suffers less from substrate variability, turbulent flow or large stones and cobbles on the river bed than optical modelling. Color and depth did affect optical model performance, but clearly less than the bathymetric SfM. The optical model accuracy improved in autumn with lower water color and turbidity (ME = −0.05) compared to spring (ME = −0.12). Correlations between the measured and modelled depth values (r = 0.96) and the models precision (SDE = 0.09–0.11) were close to those achieved with echo sounding. Shadows caused by riparian vegetation restricted the spatial extent of the optical models.

1. Introduction

In mapping fluvial environments, methods for collecting bathymetric data have not developed as rapidly as general topographic measurement techniques. This has led to a situation where dry areas of river environments are mapped with much higher detail compared to underwater areas. Some bathymetric approaches suffer from either poor spatial resolution or precision, or are not applicable in very shallow areas. The bathymetry of shallow rivers is especially complicated to measure as bathymetric measurement devices (e.g., echo sounders) have been primarily designed for the measurement of deeper waters (Dietrich, 2017). Zones of shallow flow, which are common in many rivers, have an important and distinct ecological and geomorphological function (e.g., riffles). They may also provide important and unique habitats for

various aquatic and terrestrial species. Thus, surveying shallow areas with high detail (e.g., sub-bedform scale) is essential for understanding the fluvial, morphological, and related ecological processes of the whole river environment.

In recent years, fluvial geomorphologists have used and developed several techniques to measure and model bathymetry of shallow water areas. Conventionally, terrestrial approaches such as differential GPS (Brasington et al., 2000) or total station survey (Lane et al., 1994; Milne and Sear, 1997; Koljonen et al., 2012) and more recently green wavelength LiDAR, (Kinzel et al., 2013), and echo-sounding methods (Guerrero and Lamberti, 2011; Kasvi et al., 2017b) have been used. Each approach has its strengths and weaknesses. RTK-GPS (Real Time Kinematic Global Positioning System) and total stations provide accurate data with high precision, but they commonly involve a trade-off between spatial extent and spatial resolution, leading to a discontinuous picture of the river bed and possibly to an incorrect interpretation of phenomenon such as erosion and deposition volumes (Lane et al., 1994; Westaway et al., 2001). These techniques also require physical

* Corresponding author.
E-mail addresses: elina.kasvi@utu.fi (E. Kasvi), eliisa.lotsari@uef.fi (E. Lotsari), Stuart.Lane@unil.ch (S.N. Lane).

contact with the river bed, which restricts their usage to safely wadeable areas. Physical contact with the river bed may also disturb the original topography as well as habitat features, such as fish spawning locations.

Echo-sounding is an active remote sensing method that transmits sound pulses toward the bed of a water body and calculates the depth of water based on the travelling time of the sound pulse and speed of sound in water. It was originally developed for marine applications but has been applied in inland waters for many decades (Dost and Mannaerts, 2008). Modern side-scan sonars, operating at high frequencies (>500 kHz) and producing high-resolution images (<0.1 m pixels) (Powers et al., 2015) are efficient but only applicable in relatively deep water (~>0.8 m) (e.g., Kaeser et al., 2013). ADCPs (Acoustic Doppler Current Profilers) equipped with echo sounders may be convenient for use in shallow waters, especially when operated using remotely-controlled systems (Flener et al., 2015; Kasvi et al., 2017b). Their advantage, especially compared to differential GPS, total station and side-scan sonar, is that they are able to measure both shallow and deep areas. They also provide information on flow velocity that a purely depth-measuring instrument does not. For very shallow depths (<0.2 m), however, side-lobe interference may disturb depth measurement (Yorke and Oberg, 2002). These devices do not have side-scan abilities and thus the associated spatial resolution is much poorer as compared with side-scan sonars and is directly dependent on the time available for the measurement campaign. Therefore, the quality of an ADCP-based, high-resolution bathymetric model is also dependent on the selected interpolation method.

With an attempt to increase the efficiency of bathymetric mapping, airborne bathymetric laser (ALB) scanners, originally designed for coastal and marine surveys, have also been used in fluvial environments (Hillade and Raff, 2008; Kinzel et al., 2013, 2007). Bathymetric LiDAR is a laser-based active remote sensing system that operates in the green and infra-red region of the electromagnetic spectrum. Recently, topo-bathymetric LiDARs have been used to map the entire stream network with the Experimental Advanced Airborne Research LiDAR (EAARL) approach (e.g., McKean et al., 2009; Wright et al., 2016; Tonina et al., 2018). The EAARL allows for rapid survey of large areas (tens of kilometers) over a wide range of water depths in clear water (0 to 44 m based on Tonina et al. (2018)). For various reasons, however, bathymetric LiDAR has not thus far become a popular bathymetric mapping approach among fluvial geomorphologists. First, it commonly requires an aerial view, helicopter or plane-borne, which is expensive and reduces user control over survey timing and frequency. In addition, various environmental factors, such as water clarity, vegetation and water surface waves, affect the transmission of the laser pulse through the water and thus influence the strength and shape of the return pulse (Guenther, 2007). Shallow depths have also been reported as a challenge for bathymetric LiDAR, due to the difficulty of separating water surface, water column, and bottom reflections from each other (Kinzel et al., 2007). Tonina et al. (2018), however, recently presented some promising results for EAARL surveys of shallow areas, but they did not present detailed analysis of the EAARL performance on those areas. The flying altitude, and consequently the laser footprint, ultimately restrict the spatial resolution of the data; in a recent study, Tonina et al. (2018) achieved point densities between 0.49 and 1.26 points/m^2 and the LiDAR footprint was 0.2 m with a flying altitude of 300 m. Mounting bathymetric LiDAR on unmanned airborne vehicles (ULS) (see RIEGL, 2018) increases the spatial resolution. The first experiments with bathymetric ULS in a shallow water survey (see Mandlburger et al., 2016) reported bathymetric data with a 0.1 m spatial resolution and a laser footprint of 3.5 cm, which are very promising results. Due to the high cost, it is not yet widely used in scientific applications.

Through-water photogrammetry offers an alternative for detailed airborne mapping (Shintani and Fonstad, 2017). Provided the stream bed is visible in the imagery, sufficient texture remains in the imagery for stereo-matching to work, and the imagery is close to nadir (i.e., airborne), then it is possible to apply two media photogrammetric methods to quantify stream bathymetry (Westaway et al., 2000, 2001).

However, these methods suffer from the same problem as bathymetric LiDAR as they traditionally required image acquisition by photogrammetric grade cameras mounted on planes or helicopters. In the wake of the increasing availability of cheap UAVs equipped with photogrammetrically-calibrated sensors, and developments in multi-view stereo photogrammetry that facilitate the calibration of non-calibrated sensors (specifically Structure-from-Motion, SfM), photogrammetric approaches have been increasingly used by fluvial geomorphologists (Javernick et al., 2014; Micheletti et al., 2015a, 2015b; Kasvi et al., 2017a; Shintani and Fonstad, 2017). SfM is relatively cheap and may also allow a higher spatial resolution as compared to the approaches presented thus far. It is based on visible light waves and is thus a passive remote sensing method. The resolution of aerial photogrammetry based methods is based theoretically on the image's pixel resolution on the ground, which in turn is a function of the UAV flying height, and the resolution of the CCD (charge coupled device) array of the sensor mounted on the UAV. This gives the user control over the resolution of the survey. As with other methods, there remains a trade-off between spatial extent and spatial resolution, but it is generally possible to obtain much higher resolutions (e.g., <0.05 m) over much larger areas than with other methods.

Crucially, more recent work has adapted SfM methods for the case of two media photogrammetry (Woodget et al., 2015; Dietrich, 2017; Shintani and Fonstad, 2017). Dietrich (2017) presented an approach in which the problem arising from the refraction of light when it enters the water body from the air has been eliminated through an iterative correction. Shintani and Fonstad (2017) used in situ reference measurements to create a site-specific refraction-correction factor to resolve the same problem. That said, issues remain regarding the extent to which it is possible to obtain reliable calibration of these sensors, especially if distortions in the acquired topographic surfaces are to be avoided (James and Robson, 2014; Carbonneau and Dietrich, 2017).

Optical modelling (also referred as the spectral depth approach or optical-empirical modelling) is long established for the measurement of shallow stream-bed bathymetry (Gilvear et al., 1995; Winterbottom and Gilvear, 1997; Westaway et al., 2003; Legleiter et al., 2004; Carbonneau et al., 2006; Marcus and Fonstad, 2008; Lane et al., 2010; Flener et al., 2013; Legleiter, 2016; Shintani and Fonstad, 2017). It rests upon the principle that light is absorbed as it passes through the water column and the form of this absorption follows a negative exponential function (i.e., Beer's law) (Carbonneau et al., 2006). The depth may be calculated based on single spectral band (blue, green or red) or using a (log-transformed) ratio of two bands (Williams et al., 2014). The band-ratio approaches are especially useful in areas with varying bottom substrates. Different spectral bands experience different attenuations and a change in bottom albedo affects two bands similarly, while a change in depth has a greater effect on the band with greater attenuation (e.g., Legleiter et al., 2004). Thus, the ratio values are more sensitive to depth than substrate variations (Dierssen et al., 2003; Stumpf et al., 2003). The form of the depth-reflectance relationship needs calibration and the calibration may not be constant as a function of either space (e.g., changes in bottom reflectance) or time (e.g., if the turbidity of the water column changes) (Flener, 2013; Williams et al., 2014; Tamminga et al., 2015). The method has proved to be particularly interesting where classical photogrammetry fails because of poor image texture, but can still provide some bathymetric points, which can then be used to calibrate imagery, opening up the possibility of acquiring bathymetry from historical imagery (Lane et al., 2010). The measurements can also be disturbed by the refraction of the light between two media if the images are not close to nadir. Water surface roughness and the vegetation on the river banks may also inhibit the light entering the water column. Shintani and Fonstad (2017) compared the ability of bathymetric SfM and optical modelling approaches to extract water depth in a gravel-bed river with shallow clear water. Their study highlighted the need for further research on the accuracy and feasibility of approaches used to produce bathymetric data.

Given the above review, it is clear that a number of factors will impact the choice of survey method, and these are both scientific and logistical. The characteristics of the study site, such as the size, depth, and water quality will limit which options are feasible. Aerial photogrammetry is not suitable for turbid waters where the bed is not visible. Echo sounding is difficult to apply to sites that are impossible to access by car or boat. The price of equipment may vary from tens of thousands of dollars (ADCP and remote controlled mini-boat) to just a couple of thousand dollars (a drone equipped with digital camera). Remote sensing seems to offer an appealing alternative but this method also needs ground calibration (whether of the optical models, or of the sensors used to acquire the imagery). Effective application of remote sensing methods may also need particular skills required to produce the bathymetric model and this may affect the choice of the most appropriate method.

To develop good practice in shallow river bathymetric survey, here we compare three promising remote sensing approaches to map shallow river bathymetry with a high resolution. We use: (1) bathymetric SfM; (2) a remote controlled ADCP equipped with an echo sounder; and (3) optical modelling; to create 1 m and 0.05 m resolution bathymetric models for a sand-bedded meandering river containing pools and bars. We map and model the study area both during rising spring flood with higher turbidity and hence higher water color (June 2017) and during autumn low discharge and low turbidity and color (September 2017). We compare the resultant nine bathymetric models with accurate field-based validation measurements of VRS-GNSS (virtual reference station global navigation satellite system) and ADCP. We discuss the strengths and weaknesses of the approaches and evaluate the effect of spatial resolution, depth, turbidity and color on the feasibility of each method.
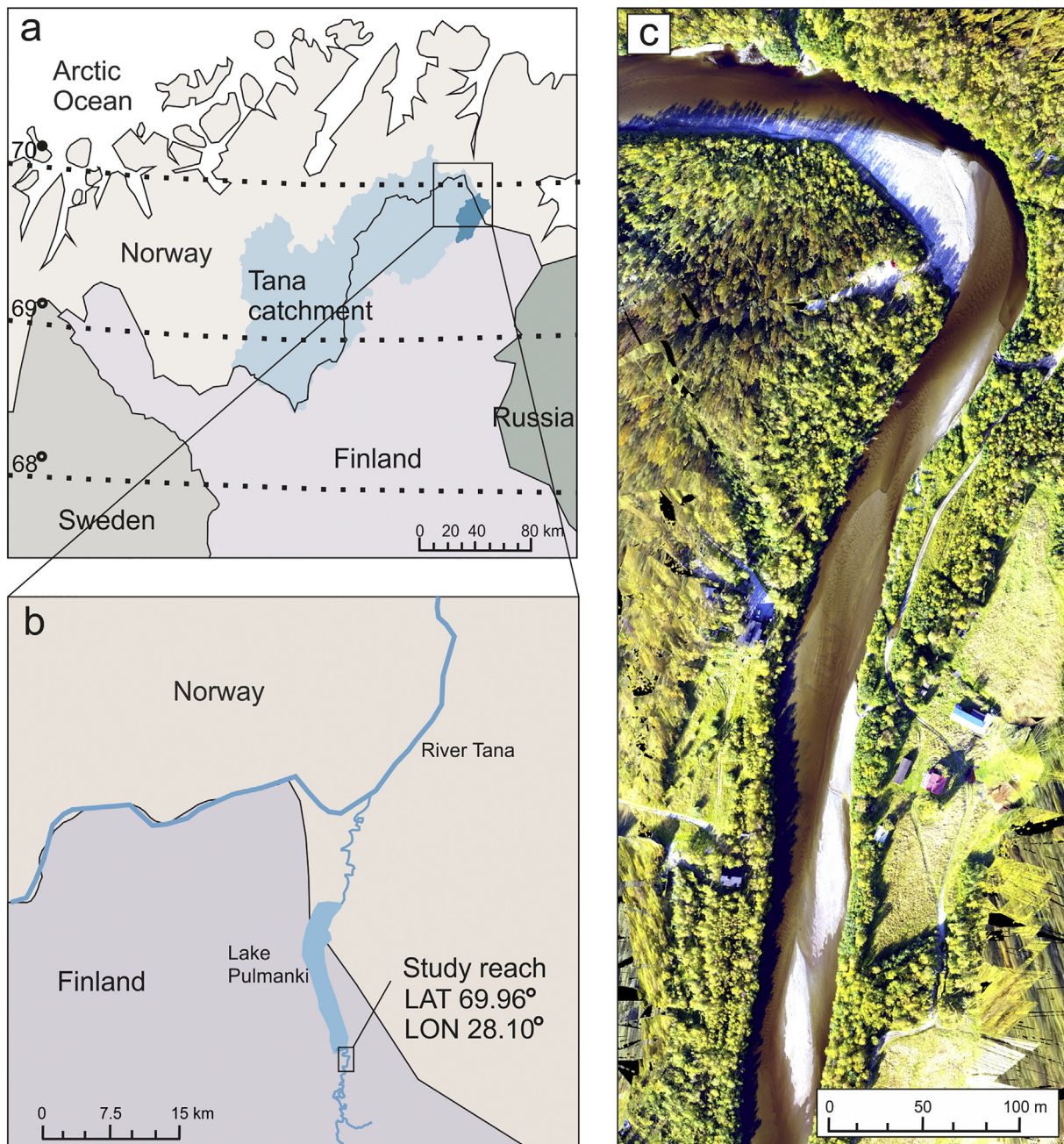

Fig. 1. (a) The Pulmanki River flows in sub-arctic Finland. The studied catchment is a part of the Tana catchment. (b) The study reach is a meandering part of the Pulmanki River, upstream of Lake Pulmanki. (c) The sand-bedded study reach has a varying bed profile with mid- and point-bars.

Table 1
Water quality in the study reach during the field campaigns.

	3–5 June	7 Sept
Discharge (m³/s)	10–15	4
Color (mg/l Pt)	55–60	35
Turbidity (FTU)	2	0

2. Study area description

The study area is located in sub-arctic Finland (Fig. 1a and b). It is a 500 m reach of the meandering Pulmanki River (Fig. 1c). The Pulmanki River is a meandering river with a sand bed (D_{50} ~0.2 to 2 mm) and discharge varying between 3 and 70 m³. Stones and cobbles are found around riffles and deeper parts art the outer banks beyond the bend apices. Typical of arctic and sub-arctic rivers, the Pulmanki River experiences annual snow-melt related spring floods that increase the turbidity of the normally clear water for some time. The study reach consists of a meander bend and a straight reach (Fig. 1c). Bedload and suspended load transport occur throughout the year, and increase along with spring flood discharges.

3. Methods

The field campaigns were performed during rising flood discharge (10–15 m³/s) on the 3–5 June and low discharge (4 m³/s) on 7 September. During the survey of 3–5 June, water level change rose 0.2 m.

3.1. Water quality measurements

Water quality measurements were performed during both field campaigns using 257.5 ml water samples taken from the study site using a depth-integrated water sampler (Table 1). The color (mg/l Pt) and turbidity (FTU) were analyzed in the laboratory with an YSI 9500 Photometer and the total suspended solids (TSS) was determined using vacuum filtering. The SSC (suspended sediment concentration) was ~6 mg/l on 3 June 2017, which suggests that the flood peak suspended load level (typically ~200 mg/l) was not yet reached, but the SSC still remained close to the low discharge level (Kasvi et al., 2013). Secchi depth was measured but not achieved. To determine the color, the sample was filtered to remove suspended solids before analysis. The color of water was expressed using the platinum/cobalt color scale (Pt/Co scale). Each unit is equivalent to the color produced by 1 mg/l platinum in the form of chloroplatinic acid in the presence of 2 mg/l cobaltous chloride hexahydrate. These units are identical with 'Hazen' units, which have been traditionally used to express results from the visual estimation of water color (YSI Inc., 2010). The turbidity analyses included filtration of one sample through a GF/B filter. This filtered sample was applied as a blank sample. The 10 ml unfiltered sample was then analyzed against this filtered blank sample. The color was analyzed by applying deionized water as the blank sample, and the filtered actual sample was analyzed against it.

Next, we created six bathymetric models (1–6) at 1 × 1 m resolution and three (4b-6b) at 0.05 × 0.05 m resolution over the study area (Table 2). The models 1–3 describe the spring time (3–5 June) bathymetry and models 4–6b the autumn (7 September) bathymetry. The three high resolution models (i.e., 0.05 × 0.05 m) were created based on the autumn data only, as the orthomosaic for the autumn was considered of better quality.

3.2. Bathymetric data collection

3.2.1. Drone-based aerial imagery

Two sets of aerial photographs were collected from the study area using a DJI Phantom 4 (DJI, 2019) in order to create georeferenced orthomosaics 1 (spring) and 2 (autumn) over the area. The Phantom 4 has a 12 megapixel camera with an aspherical lens with a 94° field of view (FOV) and 35 mm equivalent focal length of 20 mm. The device has an integrated low quality GNSS. The image collection procedures in 3 June and 7 Sept were similar. First, the ground control points (30 and 21 GCPs in the spring and autumn, respectively) were installed to cover the whole survey area as evenly as possible and their exact locations were measured using VRS-GNSS for geo-referencing purposes. It has been shown that multiple flight altitudes should diminish the probability of systematic error such as doming (Carbonneau and Dietrich, 2017) and thus three sets of images were collected; one at 90 m (nadir), one at 70 m (nadir) and one at 50 m (off-nadir, 30° off vertical) above the ground. Two flight lines, i.e., back and forth, were flown at each altitude, flying first along the right bank and then back along the left bank of the river. Time lapse imaging was used and the interval was set as 2 sec. Despite flying along the banks, each flight line covered the whole submerged channel area (width of the channel ~20–30 m during both measurement dates). Thus, the overlapping coverage of the aerial imagery was excellent. After creating orthomosaics 1 and 2 (see Figs. 2 and 3) they were used to create six bathymetric models: orthomosaic 1 was used to create SfM_S_1m (1 m resolution bathymetric SfM for spring) and Optical_S_1m (1 m resolution optical model for spring), while orthomosaic 2 was used for SfM_A_1m and SfM_A_0.05 m (1 m and 0.05 m resolution bathymetric SfM for autumn), and for Optical_A_1m and Optical_A_0.05 m (1 m and 0.05 m resolution optical models for autumn) (Table 2).

Table 2
Data collected for the 1 × 1 m and 0.05 × 0.05 m bathymetric models. DSM = Digital Surface Model (see Section 3.2).

| Spring 2017 (mid-flow)		Autumn 2017 (low-flow)	
SfM_S_1m		SfM_A_1m	
		SfM_A_0.05 m	
Source data	Orthomosaic 1	Source data	Orthomosaic 2
Original cell size	0.034 m	Original cell size	0.028 m
Original point density	865 points/m²	Original point density	1275 points/m²
ADCP_S_1m		ADCP_A_1m	
		ADCP_A_0.05	
Source data	3880 echo sounding points	Source data	3525 echo sounding points
	VRS-GNSS measurements		Differential GPS measurements
Original point density	0.63 points/m²	Original point density	1.3 points/m²
Optical_S_1m		Optical_A_1m	
		Optical_A_0.05 m	
Source data	Orthomosaic 1	Source data	Orthomosaic 2
Calibration data	48 RTK-GNSS points	Calibration data	48 RTK-GNSS points
	91 echo sounding points		91 echo sounding points
Original cell size	0.034 m	Original cell size	0.028 m
Original point density	865 points/m²	Original point density	1275 points/m²
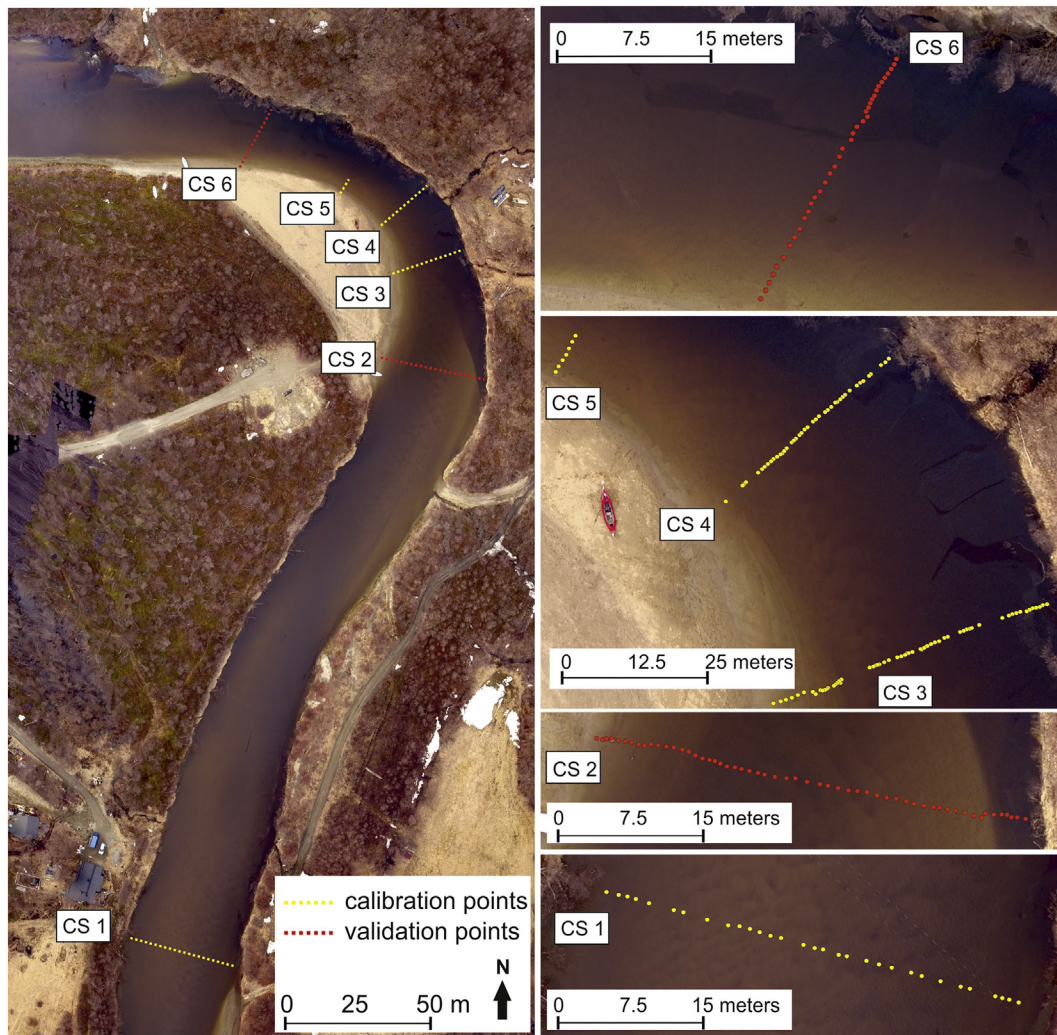
Fig. 2. Orthomosaics and the calibration and validation points for the spring. The yellow calibration points (CS 1, 3, 4 and 5) were used in building Optical_S_1m. The red validation points (CS 2 and 6) were used to validate all of the spring models.

3.2.2. Echo sounding with ADCP

Echo sounding-based bathymetry data were collected using an ADCP (Sontek RiverSurveyor M9 and S5) attached to a remote controlled mini-boat on 5 June (M9) and with a kayak on 7 September (S5) over the study area. Thus, the spring ADCP data were measured two days after the drone flights and validation data measurements. Meanwhile, the water level had risen 0.2 m. The issue of the data being from different dates is acknowledged in the analysis as the river bed may have evolved and the inundated area may have been slightly larger during the ADCP survey compared to other data. With the RiverSurveyor M9 and S5 the flow depth is recorded by a vertically-oriented echo sounder operated at 0.5 MHz and 1 MHz, respectively. The manufacturer reports a depth measurement accuracy of 1% for both M9 and S5 sensors (Sontek, 2016). The position of the spring depth points was measured using VRS-GNSS (Trimble R10), but in the autumn only the ADCP's differential GPS (dGPS) was used. The VRS-GNSS system enables more precise location (horizontal accuracy <0.05 m) of the measurements, compared to the dGPS (horizontal accuracy of sub-meter scale, Sontek, 2016). As the spring measurement was not performed at the same time as the flights and the reference measurements, we were able to use the VRS-GNSS in the wider measurement campaign. During the autumn field campaign, the ADCP measurements were performed simultaneously with rest of the data gathering, and so the VRS-GNSS was not available for the time-intensive ADCP measurement. The VRS signals depend on an internet connection, and especially in remote areas such

as our study area, problems with connections occur. Receiving the VRS signal may take considerable amounts of time. The accuracy of the dGPS was tested: a stationary measurement of 10 min was used to quantify coordinate variations at a fixed point. The maximum differences from the mean x, y coordinate values were 0.08 m and 0.23 m and the standard deviations were ± 0.04 m and ± 0.10 m.

Both the ADCP and VRS-GNSS measurements were recorded with 1 Hz frequency and the density of the depth soundings depended on the boat speed. The achieved point densities were 0.63 and 1.3 points m^{-2} in the spring and the autumn, respectively. The lower point density in the spring was mainly caused by the large areas of shallow but inundated point bars, which were too shallow (<0.2 m) for the ADCP depth measurements. In the autumn, the point bars were exposed due to the lower water surface elevation and the main channel was mostly deep enough for the ADCP measurements and thus higher point density over the surveyed area was achieved. The RS mini-boat system is described in detail by Kasvi et al. (2017b).

3.2.3. Calibration and validation data

Calibration and validation data were collected along six cross sections using both VRS-GNSS (shallow areas) and ADCP (Riversurveyor M9, areas over 1.2 m in depth) in the spring (Fig. 2) and the autumn (Fig. 3). The VRS-GNSS measurements were collected by walking from the shallow inner bank of the bends toward the outer bank until the water was too deep for the VRS-GNSS measurements (1.2 m). ADCP

Fig. 3. Orthomosaics and the calibration and validation points for autumn. The yellow calibration points (CS1, 3 and 5) were used in building the optical models of the autumn. The red validation points (CS2 and 6) were used to validate all of the autumn models.

measurements were used to continue the cross section across the whole river to the outer bank. ADCP data were collected using the remote controlled boat equipped with the ADCP device and VRS-GNSS. The time available to complete the calibration and validation measurements was limited as these data were collected simultaneously with the drone flights to avoid the changes in river bed and water level during the surveys. Furthermore, the crew taking reference measurements needed to stay out of the water when the drone passed by. Cross sections 1, 3, 4 and 5 were used to calibrate the optical models. In total, 48 VRS-GNSS and 91 ADCP calibration measurements with an average

point spacing of 0.86 m were collected in the spring and the autumn for that purpose. Cross sections 2 and 6 were used to validate each bathymetric model. In total, 93 and 54 validation measurements were collected in the spring and autumn, respectively.

3.3. Bathymetric data processing

3.3.1. Aerial images: creating orthomosaics and DSMs

Two orthomosaics and DSMs were created using SfM photogrammetry, which is based on matching features in multiple overlapping

Table 3
The quality details of the calibration, bundle adjustment and georeferencing of orthomosaics 1 and 2.

	Orthomosaic 1 3 June	Orthomosaic 2 7 Sept
Average ground sampling distance (m)	0.034	0.028
Median of key points per image	27,585	37,411
Total number of images	1270	1746
Images calibrated (%)	98	98
Number of GCPs	30	21
Mean reprojection error (pixels)	0.216	0.19
Relative difference between initial and optimized camera parameters (%)	2.11	2.47
Mean RMS error of GCPs (m)	0.035	0.039

images acquired from multiple viewpoints (James and Robson, 2012; Westoby et al., 2012). The SfM method determines the camera position, orientation, lens distortions and focal length automatically using a bundle adjustment. Orthomosaics and DSMs were created for both spring (orthomosaic 1, DSM 1) and autumn (orthomosaic 2, DSM 2). The processing of image sets for the spring and autumn was identical. The orthomosaics and DSMs were created and georeferenced in the commercially available Pix4D software package. The general steps of the SfM procedure can be found in, for example, Micheletti et al. (2015a). In total, 30 and 21 GCPs were used for the spring and autumn, respectively. The number of overlapping images was five or more for the whole study area in both spring and autumn. The orthomosaic quality is summarised in Table 3.

3.3.2. Echo sounding data

For the echo sounding data of 5 June, the accurate locations of the echo-sounding points were calculated based on post-processed VRS-GNSS measurements. Post-processing was done with virtual correction data provided by the Finnish virtual reference station network, which allows horizontal precision of ±0.05 m. Echo soundings and VRS-GNSS values were combined based on UTC time stamps of the VRS-GNSS and the ADCP's internal dGPS. As only the ADCP's internal dGPS was used on 7 September, no pre-processing was needed for the bathymetry points.

3.4. Bathymetric modelling

3.4.1. SfM-based bathymetric modelling

The SfM-based bathymetric models for the spring (SfM_S_1m) and autumn (SfM_A_1m and SfM_A_0.05 m) were created using the approach presented by Dietrich (2017) based on Westaway et al. (2001). In this approach, the problem arising from the refraction of light when it enters a water body (refractive index = 1.337, (Harvey et al., 1998)) from the air (refractive index = 1.0) is dealt with using an iterative multi-camera refraction correction. The correction is calculated for each point-camera combination of points falling in the inundated area. The approach solves for the actual depth of the water body based on the refractive indexes of air and water, angle of the refraction, angle of incidence from the stream bed to the air/water interface and the apparent depth based on the DSM and water-surface elevation. The correction algorithm requires the orthomosaic, DSM and a water-surface elevation model restricted to the inundated area, and corrected camera positions with pitch and roll. Based on the camera position and the FOV, the points in the point cloud that are visible to the camera can be calculated and all of the point-camera combinations defined. A full technical description of the approach can be found in Dietrich (2017). According to his study, the approach is capable of producing bathymetric datasets with accuracies of ~0.02% of the flying height and precisions of ~0.1% of the flying height in ideal conditions.

In this study, the inundated area was defined by measuring the water edge with VRS-GNSS in the field. The same data were used to create a raster describing the water-surface elevation of the study area. The water level stayed stable (±2 cm) during the survey. The orthomosaic and DSM were clipped to include only the wetted area. The camera positions and orientations (i.e., pitch and roll) based on the calculations in Pix4D, were further used to calculate the angles of incidence and refraction. The resulting point clouds, containing the depth points with horizontal location in the same spatial resolution as the input data (see Table 3), were interpolated to 1 m and 0.05 m resolution bathymetric rasters using kriging (see Fig. 4a for the SfM_S_1m, Fig. 5a for SfM_A_1m, and Fig. 5d for SfM_A_0.05 m).

Subsequently, the models were filtered using a Chauvenet-type criterion to identify data outliers (e.g., Micheletti et al., 2015b). The approach attempts to find outliers (i.e., erroneous/clearly deviating pixels) by comparing the depth values of each pixel with the measured
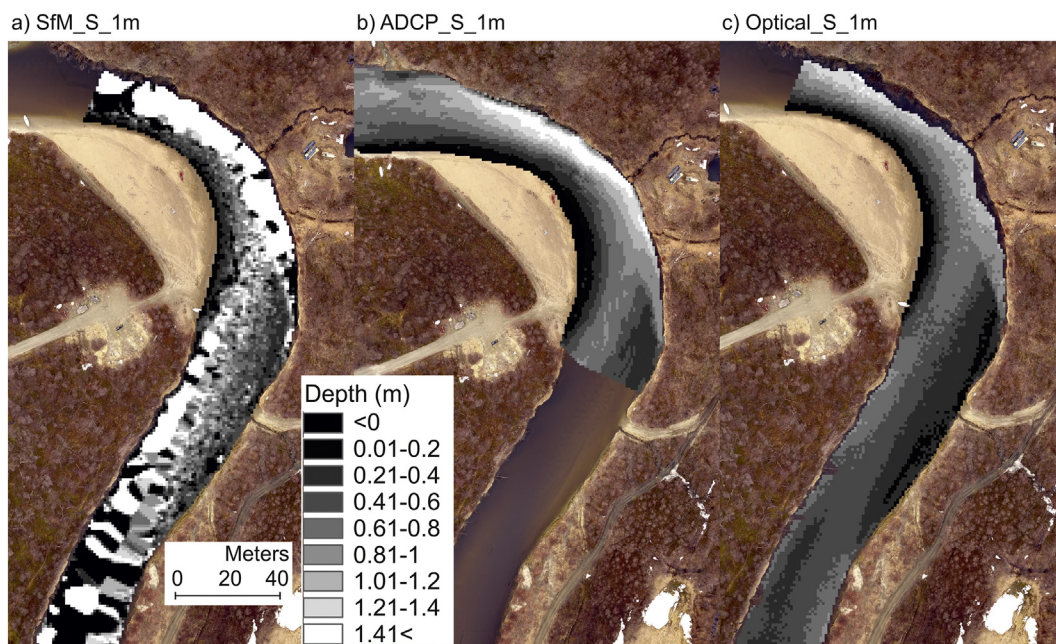

Fig. 4. Bathymetric models of 1 m resolution for spring 2017. (a) SfM_S_1m. (b) ADCP_S_1m. (c) Optical_S_1m.

a) SFM_A_1m b) ADCP_A_1m c) Optical_A_1m

Depth (m)
<0
0-0.2
0.2-0.4
0.4-0.6
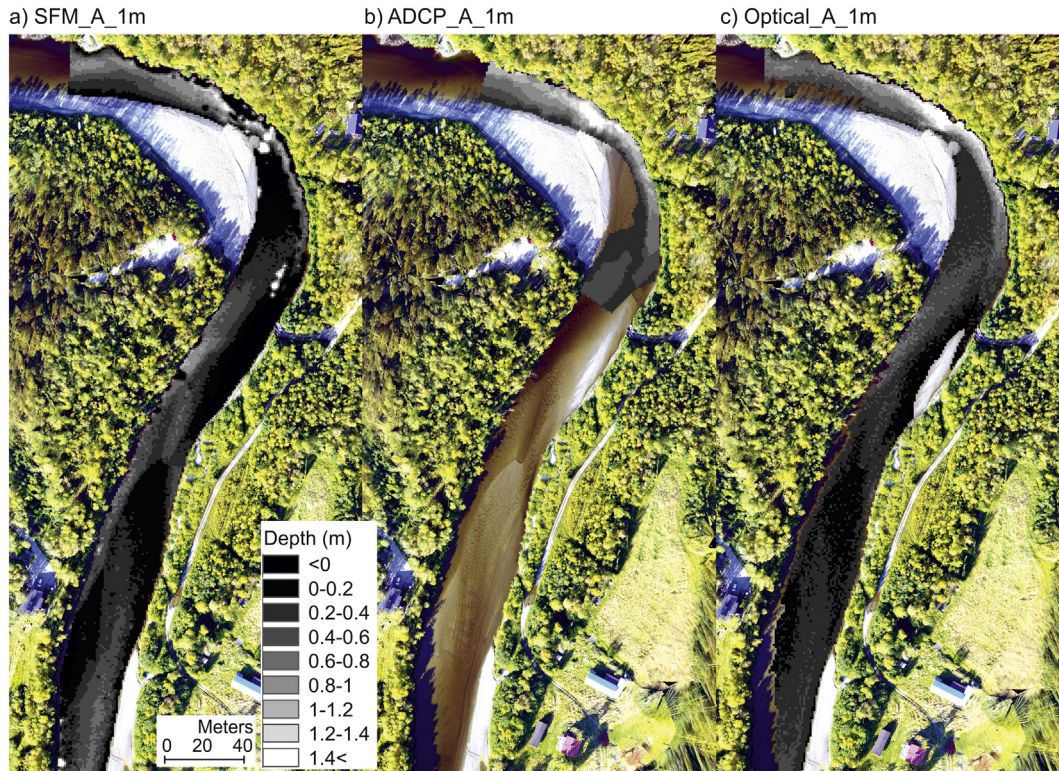0.6-0.8
0.8-1
1-1.2
1.2-1.4
1.4<

Meters
0 20 40

Fig. 5. Bathymetric models of 1 m resolution for autumn 2017. (a) SfM_A_1m. (b) ADCP_A_1m. (c) Optical_A_1m.

standard deviation of the surrounding data. Each pixel value (Z) in the bathymetric rasters (SFM_S_1m, SfM_A_1m and SfM_A_0.05 m) was evaluated and considered as an outlier if:

$$|Z - \overline{Z}| > 1.96 \sigma_z \tag{1}$$

where Z is the pixel value at the center of a circle-shaped neighbor with mean elevation $\overline{Z}$ and standard deviation σ_z, both calculated excluding the point of interest. The radius of the circle was 3 m and 1 m for the 1 m and 0.05 m resolution models, respectively. Any cell center falling inside the circle was included in the processing. As a consequence of the filtering, 2.2%, 1.8% and 1.3% of the pixels were removed from models SfM_S_1m, SfM_A_1m and SfM_A_0.05 m, respectively. The outliers were not used in the quality assessment.

3.4.2. ADCP-based bathymetric modelling

The echo-sounding points from spring and autumn, with the x and y coordinates, were interpolated to 1 m (ADCP_S_1m and ADCP_A_1m) and 0.05 m (ADCP_A_0.05 m) resolution bathymetric rasters using the ordinary Kriging interpolation method (see Fig. 4b for ADCP_S_1m and Fig. 5b for ADCP_A_1m). A spherical semivariogram model and a search radius of 12 points was used in the interpolation. Due to the higher discharge and water level in the spring compared to the autumn, ADCP_S_1m had slightly larger spatial coverage compared to ADCP_A_1m and ADCP_A_0.05 m. The spatial coverages of the models were defined based on the point measurements by digitizing the area along the points closest to the banks.

3.4.3. Optical bathymetric modelling

Both single-band and band-ratio approaches were tested. The band-ratio approaches in Experiment 3 of Williams et al. (2014) were applied, but a single-band (red) linear transform was used for the depth calculations as it provided the best correlation. The approach applied was originally developed by Lyzenga (1981), but modified by Flener (2013). The Lyzenga approach attempts to isolate the depth signal in the aerial

image and linearize the relationship between observed brightness and depth. For this, it determines the radiance of a location where the water is deep enough for the river bed not to influence on the radiance. This is called deep-water radiance (L_{si}) and it is then subtracted from the radiance of each pixel. The natural logarithm of the resulting value gives a Lyzenga number, X_i, which is then calculated for each band (red, green and blue):

$$X_i = \ln(L_i - L_{si}) \tag{2}$$

where L_i is the digital number of the pixel in the same band. The model equation is determined by applying a regression curve of the X_i values to the calibration depth measurements. However, calculating the deep-water radiance requires that there are image pixels where the river bed is not visible. Thus, Flener (2013) modified the Lyzenga (1981) algorithm to estimate the L_{si} in shallow rivers where it cannot be retrieved from the imagery as the flow is everywhere too shallow. In his study, he found that there is no difference between the model including the estimated L_{si} and the one assuming it to be negligible. Therefore, in this study, we applied the optical model based on Lyzenga's (1981) work but we neglected the L_{si} following Flener's (2013) work.

First, we digitized the model areas on the orthomosaics 1 and 2 so that they contained no dry areas or shadows caused by tree canopies and vegetation, as those affect the pixel brightness and cause error in the regression curve. Next, the clipped orthomosaics were resampled to diminish the noise caused by ripples on the river bed: orthomosaic 1 was resampled to a 1 m and orthomosaic 2 to 1 m and 0.05 m resolution images. The new pixel values were based on nearest neighbor. We calculated the X_r (Lyzenga number for the red band) for each pixel in the images as follows:

$$X_r = \ln(L_r) \tag{3}$$

where L_r is the digital number of the pixel in the red band. For those pixels with existing calibration depth measurements, we regressed

Table 4
Statistical characteristics describing the quality of the bathymetric models 1-6b. Correlations marked with red color are not statistically significant. ME = mean error, MAE = mean absolute error, SDE = standard deviation of error.

	Model	r	R^2	ME (m)	MAE (m)	Min. error (m)	Max. Error (m)	SDE (m)	n
Spring	SfM_S_1m	0.75	0.56	1.37	1.46	−0.59	15.76	±2.88	77
	ADCP_S_1m	0.97	0.94	−0.02	0.07	−0.29	0.23	±0.08	93
	Optical_S_1m	0.96	0.92	−0.12	0.13	−0.27	0.34	±0.09	93
Autumn	SfM_A_1m	−0.10	0.01	−0.30	0.30	−2.41	−0.05	±0.50	54
	ADCP_A_1m	0.98	0.96	−0.01	0.05	−0.23	0.24	±0.07	52
	Optical_A_1m	0.96	0.92	−0.05	0.09	−0.26	0.18	±0.11	47
	SfM_A_0.05 m	0.01	0.00	−0.31	0.31	−3.00	−0.03	±0.56	54
	ADCP_A_0.05 m	0.98	0.96	−0.02	0.05	−0.24	0.24	±0.07	52
	Optical_A_0.05 m	0.96	0.92	−0.06	0.09	−0.26	0.09	±0.10	47

the X_r values against the depth (D) values. In total, 131 (spring) and 127 (autumn) calibration points were used with depth variations of 0.04–1.66 m (spring) and 0.02–1.80 m (autumn). The regression results obtained were:

$$D_s = -1.8845X_{rs} + 9.4133 \qquad (4)$$

$$D_a = -0.9108X_{ra} + 4.6439 \qquad (5)$$

$$D_{a2} = -0.9597X_{ra2} + 4.8509 \qquad (6)$$

where X_{rs}, X_{ra}, and X_{ra2} are the X_r values of spring 1 m, autumn 1 m and autumn 0.05 m orthomosaics, respectively. Eqs. (4)–(6) were then used to model depth for each pixel in the images based on the X_r values. The modelled depth values were used to create 1 m (Optical_S_1m and Optical_A_1m) and 0.05 m (Optical_A_0.05 mb) resolution bathymetric raster models.

3.5. Quality assessment of the bathymetric models

To investigate bathymetric quality, we compared the depth values of each model with the point type validation data of cross sections 2, 4 and 6 in the spring (Fig. 2) and 2 and 6 in the autumn (Fig. 3). We compared the models against the whole validation dataset to analyze the accuracy and precision of each model (Table 4, Figs. 6 and 7). To assess the accuracy, we calculated the mean error (ME) and mean absolute error (MAE), and to assess precision we calculated the minimum and maximum errors and the standard deviation of error (SDE) (Westaway et al., 2001). We also calculated the correlation coefficient (r) and R^2. To investigate the effect of depth on data point quality, the measured depth values were plotted against the modelled depth values as well as the absolute modelling error of that point (Figs. 6 and 7). The points with a modelled depth error <0.2 m were highlighted with orange. Based on visual interpretation, three error clusters were identified. To find explanations of the reasons for identified error clusters and the location of the errors in the study area, the measured and modelled values were plotted on the validation cross sections (Fig. 8) and the points with modelling errors larger than 0.2 m were visualized on an orthomosaic (Fig. 9). The error statistics were calculated separately also for each cross section and dataset (Table 6).

4. Results

4.1. Qualitative assessment

The bathymetric models were created for the spring and autumn as their hydrological conditions are usually different. The actual difference was lower than expected (10 m³/s versus 4 m³/s), although the discharge rose rapidly after the 3 June survey (to 72 m³/s by 9 June). As the water quality measurements suggest (Table 1), the water was much clearer and the visibility of the river bed in the aerial photographs was better in the autumn (Fig. 3) compared to the spring (Fig. 2).

This is also evident in comparing SfM_S_1m (spring - Fig. 4a) and SfM_A_1m (autumn - Fig. 5a), based on the bathymetric structure from motion. SfM_S_1m is noisy and the deep parts closer to outer bank seem to be poorly modelled. However, the poorly modelled upstream part of SfM_S_1m is not explained by deep water. On the basis of visual interpretation, the models based on ADCP data and optical modelling differ much less from each other, and their coherence suggests that they are both likely to be more reliable. The other striking difference between the models is their spatial extents. Especially in the autumn (ADCP_A_1m and ADCP_A_0.05 m) the models are spatially restricted because of the difficulties of ADCP survey of very shallow zones (Fig. 5). The shallowest part of the study area, almost the entire point bar head, is executed from the model.

The point density of the Orthomosaic 2 (autumn) was 1275 points/m², which is notably higher compared to the ADCP point density (1.3 points/m²). The formation of the ADCP-based 0.05 m bathymetric model (ADCP_A_0.05 m) required heavy interpolation, contrary to the photogrammetric models (SfM_A_0.05 m and Optical_A_0.05 m). Fig. 6 illustrates the bathymetric variability in the river bed captured by orthomosaic 2 and the extent to which the models can pick up the finer resolution bathymetric information. The bathymetric variability is evident in the orthomosaic (Fig. 6a). The bedforms are especially clear at the upstream part of the bend (Fig. 6i), while at the downstream part, the bed structure is smoother (Fig. 6e). As expected, SfM_A_0.05 m and Optical_A_0.05 m show much more bathymetric variability compared to ADCP_A_0.05 m. The ripples, evident in Fig. 6i, are only reproduced by Optical_A_0.05 m (Fig. 6l). Also, SfM_A_0.05 m shows bathymetric variability, which does not represent the bedforms effectively (Fig. 6j). The bathymetric variability of the 0.05 m resolution models evident in Fig. 6, are illustrated also in Fig. 7: the vertical profiles of SfM_A_0.05 m and ADCP_A_0.05 m are much smoother compared to Optical_A_0.05 m. It is also evident, based on Fig. 7, that the small-scale bed structures are not reproduced by the validation data.

4.2. Quantitative assessment

As the visual interpretation of SfM_S_1m and SfM_A_1m suggested that SfM_S_1m had poorer quality in terms of the error statistics, even though the correlation of 0.68 was statistically significant (Table 4). SfM_S_1m had the largest ME (1.03 m) and MAE (1.37 m) of all the models. The maximum error was as high as 15.75 m. This suggests that the filtering of outliers in the SfM models may not have been sufficient. The increase of the model resolution in autumn did not appreciably impact the SfM model (Models 4 and 4b) statistics. All of the errors in SfM_A_1m and SfM_A_0.05 m were negative. Interestingly though, the SDE of SfM_A_0.05 m (±0.56 m) was slightly poorer than that of SfM_A_1m (±0.50 m). In spring, ADCP_S_1m and Optical_S_1m were similarly precise, having very similar SDEs, even though ADCP_S_1m was clearly more accurate (ME = −0.02 and −0.12 for ADCP_S_1m and Optical_S_1m). The same phenomenon was noticeable but not as clear in the autumn with the ADCP-based and optical models. Thus, the ADCP-based models were accurate but not as precise, the error
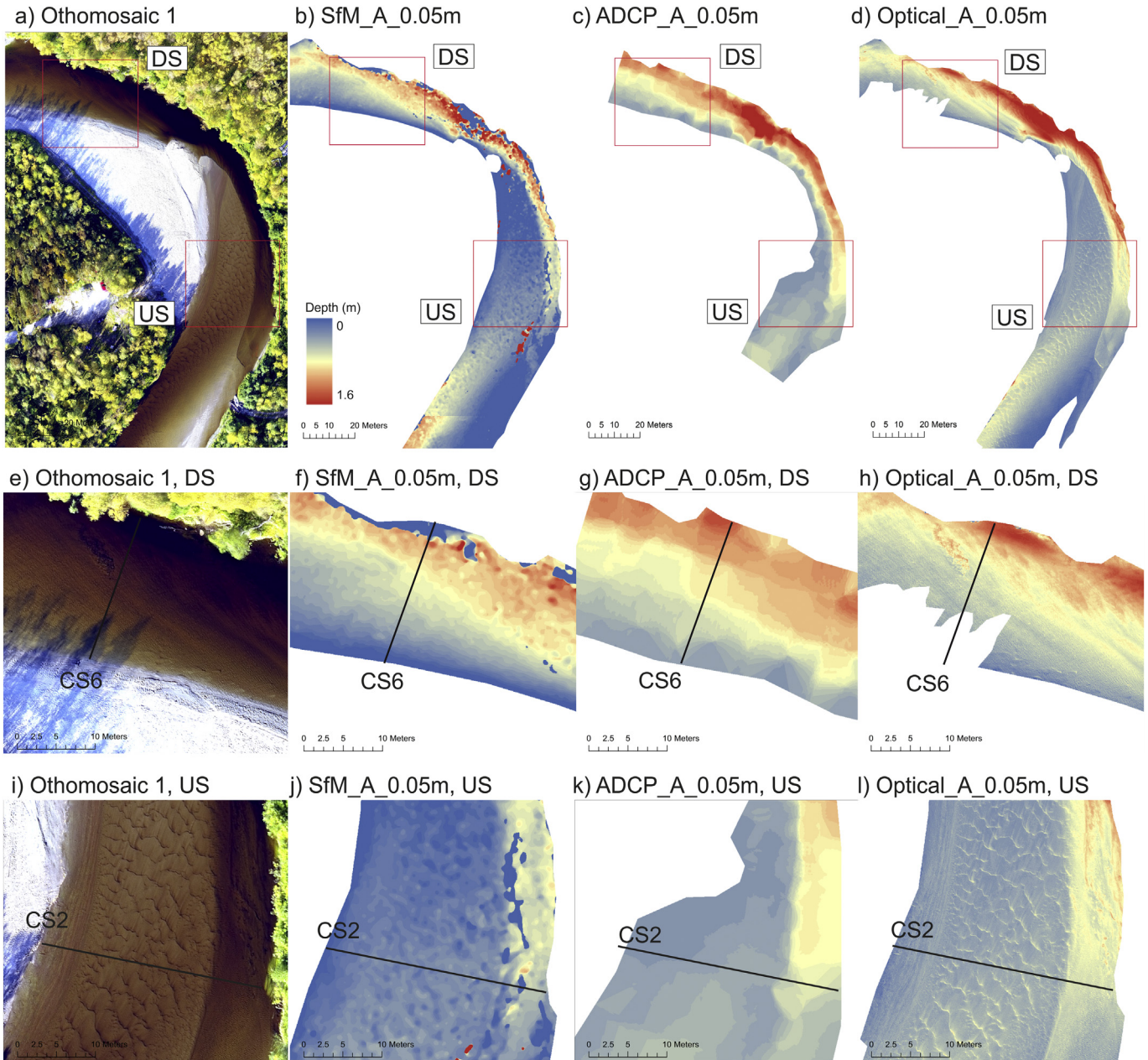
Fig. 6. Othomosaic and the bathymetric models of 0.05 m resolution for autumn 2017. (a–d) the entire area of interest. The red rectangles delineate the inspection windows at downstream (DS) and upstream (US) part of the bend. (e–h) The inspection windows at the downstream part of the bend. (i–l) The inspection windows at the upstream part of the bend.

magnitudes ranged approximately between −0.25 and 0.25 on each ADCP-based model.

Generally, the ADCP-based models were accurate and had good correlations with the validation data points. The mean errors were −0.02 m, −0.01 m and −0.02 m for models ADCP_S_1m, ADCP_A_1m and ADCP_A_0.05 m, respectively. The difference between ADCP_S_1m and ADCP_A_1m is most probably explained by the higher point density of the autumn data (1.3 points m^{-2}) compared to spring (0.63 points m^{-2}). Furthermore, the increased resolution in the autumn from 1 m in ADCP_A_1m to 0.05 m in ADCP_A_0.05 m slightly decreased the accuracy of the model. Correlations were 0.97 or higher in each case.

The optical model errors for autumn were negatively biased (Table 4). The clearest effect of increasing the model resolution was found in the optical model: the maximum error in Optical_A_0.05 m is only half the magnitude compared to Optical_A_1m. Otherwise the statistics of Optical_A_1m and Optical_A_0.05 m do not differ

much. In general, the optical models for autumn were more accurate (ME = −0.05 m and −0.06 m for Optical_A_1m and Optical_A_0.05 m respectively) compared to the spring optical model (ME = -0.12 m) even though the correlations were the same for each optical model (0.96). The accuracy was also slightly poorer compared to the ADCP-based models, although this might be compensated by the fact that Optical_S_1m and Optical_A_1m provide continuous topographic coverage at a higher density, thus reducing errors associated with sampling density.

4.3. Effect of depth on the model validity

Visual appraisal revealed that in spring, SfM_S_1m did perform substantially better for depths <0.8 m compared to deeper areas, where errors up to 1200% appeared (depths around 1–1.2 m, Fig. 8a and d, error cluster #1). However, the filtering did not remove these points.
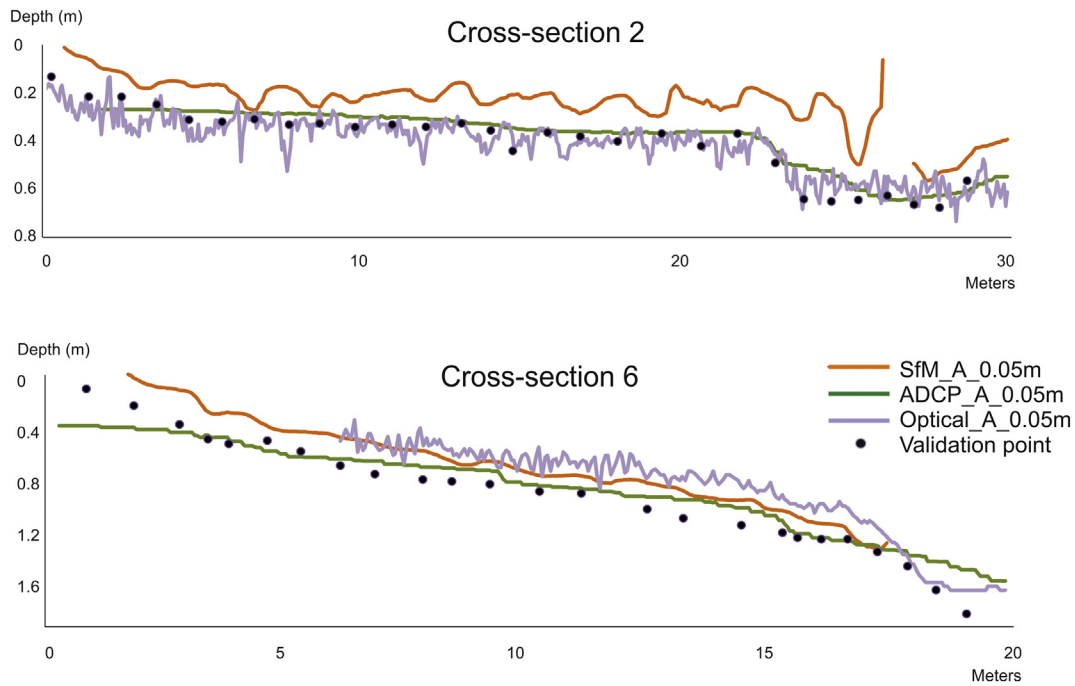
Fig. 7. Cross-sectional data for the 0.05 m resolution bathymetric models (SfM_A_0.05 m, ADCP_A_0.05 m and Optical_A_0.05 m) for autumn 2017. The depth values are extracted in 0.05 m resolution. (a) Cross section 2. (b) Cross section 6.

Therefore, the model was manually filtered further: the modelled depths on areas deeper than 0.8 m were removed from the validation point locations of SfM_S_1m and SfM_A_1m. Points with negative modelled depth values also were removed as they were clearly erroneous. Table 5 represents the statistics of the manually-filtered SfM data. In total, 48% and 24% were removed from the spring and autumn data points, respectively. In both models, approximately 10% of the validation comparison points were negative. Only a few points with negative modelled depth values were located in areas with <0.8 m depth (Figs. 8 and 9). Thus, the implications of removing the negative values for mapping are not marked. The filtering diminished the ME from 1.37 m to 0.11 m and SDE from ±2.88 m to ±0.26 m for SfM_S_1m. The ADCP_S_1m produced only a few points where the error was >0.2 m (Fig. 8b). The errors were random and there was no indication of a depth-dependence of the errors (Fig. 8e). The errors of Optical_S_1m were equally distributed across the depths present and no depth-dependence was evident (Fig. 8c and f).

SfM-based SfM_A_1m (Fig. 9a) performed better compared to SfM_S_1m (Fig. 8a) as the ME and SDE suggested (Table 4). A cluster of errors appeared around depths of 0.5 m (Fig. 9a and d, error cluster #2). There are also some points located in the deepest areas of the river (depths 1 to 1.4 m), that had negative depth values in SfM_A_1m (Fig. 9a and d, error cluster #3). In the error cluster #3, errors of up to 190% occurred. These negative values explain the negative correlation of SfM_A_1m. Even though a less clear depth-dependence is present in the errors of SfM_A_1m compared to SfM_S_1m, excluding the depths over 0.8 m and the negative modelled depths diminished the ME from −0.30 m to −0.15 m and the SDE from ±0.50 to ±0.09 for SfM_A_1m (Table 5).

Models ADCP_A_1m and ADCP_A_0.05 m, as the correlations suggested, performed well (Fig. 9b). Only a few errors appeared in the very shallow (depths <0.2 m) areas and also in the deepest areas (depths around 1.4 m). The shallow area errors are explained by the fact that the ADCP is incapable of measuring depths under 0.2 m. As with ADCP_S_1m, all of the modelling errors of ADCP_A_1m were <0.25 m. Also Optical_A_1m performed well with no clear depth-dependent error clusters (Fig. 9c and f).

4.4. Spatial patterns of error

In spring, in cross section 2, SfM_S_1m had mostly over-estimated the depth values in areas with depths >0.5 m (Fig. 10a). The correlation between the modelled and measured depths was 0.58 (Table 5). SfM_S_1m had better correlation with the measured data in cross section 6 ($r = 0.72$) but Fig. 10b shows that error magnitudes were of the order of several meters on the deeper part of the section. Also, the accuracy and precision of SfM_S_1m was notably better in cross section 2 (ME = 0.13 m, SDE = ±0.34 m) compared to cross section 6 (ME = 3.2 m, SDE = ±4.03 m). The largest errors of SfM_S_1m were found in both cross sections 2 and 6, in areas deeper than 1 m, near the right bank of the river (Fig. 10a and b, 11a and b). This area is also where error cluster #1 appeared (Fig. 11a and c). By looking at Fig. 11a and c it is clear that these are where the river bed is poorly visible in the orthoimages. However, fewer such deep points were present in cross section 2.

ADCP_S_1m and Optical_S_1m slightly under-estimated the depth values in both cross sections (Fig. 10a and b). The correlations of ADCP_S_1m were 0.94 and 0.99 in cross section 2 and 6, respectively (Table 6). For Optical_S_1m, the corresponding correlations were 0.93 and 0.99. Thus, on the basis of correlation, the ADCP and Optical model produced very similar results. They were also similarly precise: the SDE was ±0.08 m and ±0.07 m for ADCP_S_1m and ±0.09 m and ±0.07 m for Optical_S_1m in cross sections 2 and 6, respectively. Accuracy showed larger variations: ME was −0.03 m and 0.00 m for ADCP_S_1m and −0.08 m and −0.17 m for Optical_S_1m in cross sections 2 and 6, respectively. The errors were mostly between −0.3 m and 0.3 m for both models. The poorer accuracy of Optical_S_1m is emphasized in cross section 6 with a correlation of 0.99 and ME of −0.17 m. In cross section 2, the ADCP data fails to reproduce the pool approximately 13 m from the left bank (Fig. 10). Instead of being a measurement error, this is most probably a consequence of the difference in the survey date, as the pool may have filled up after the validation measurements were taken.

In the autumn, SfM_A_1m under-estimated the depth values in cross section 2 by about 0.1 to 0.2 m (Fig. 10c). The most notable errors occurred with a sudden increase in depth at 20 m from the left bank,
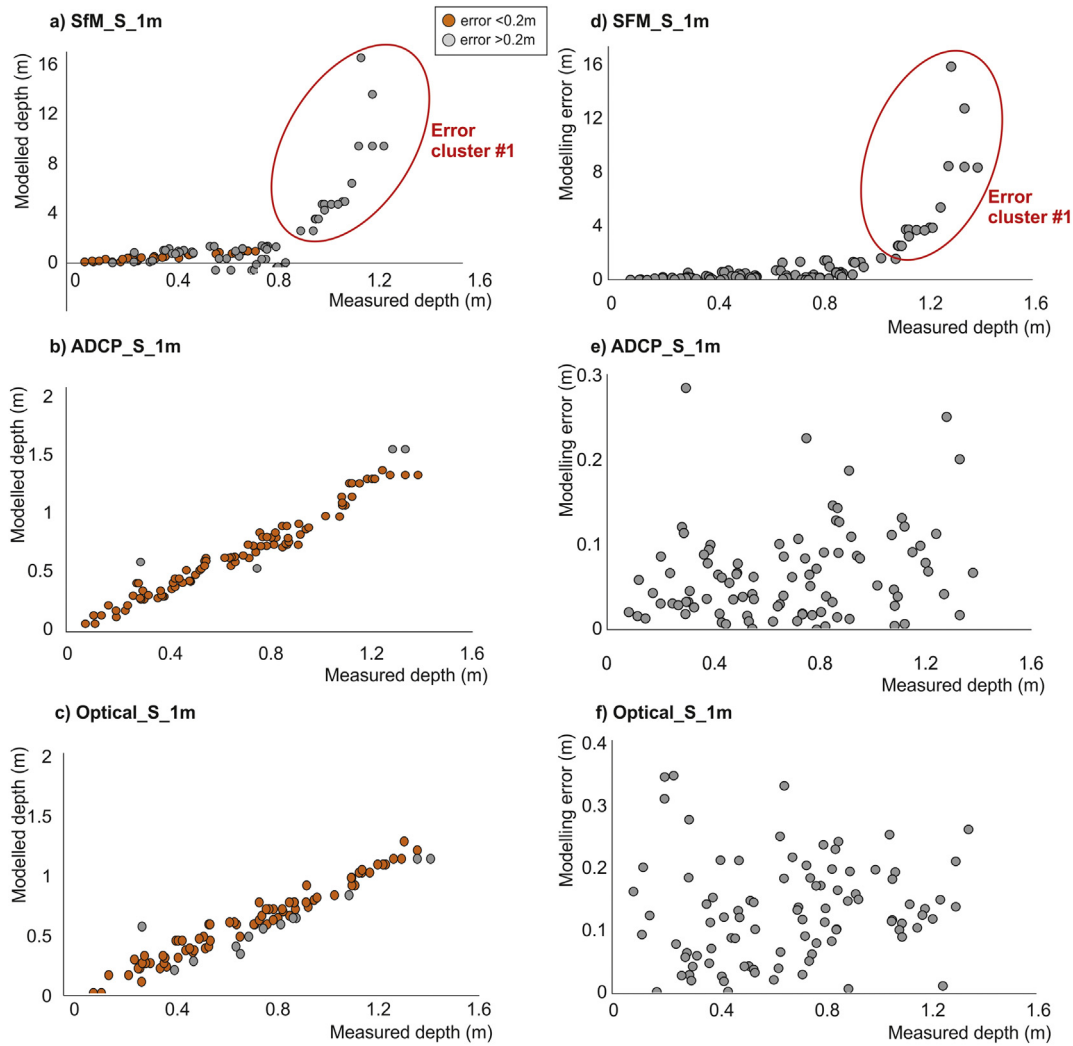
Fig. 8. (a–c) Spring measured depths plotted against modelled depth for the 1 m resolution models (a) SfM_S_1m, (b) ADCP_S_1m, and (c) Optical_S_1m. The orange plots describe model values that fall within 0.2 m of the validation depth measurements. (d–f) Spring measured depth plotted against the absolute error of the modelled depth value for (d) SfM_S_1m, (e) ADCP_S_1m, and (f) Optical_S_1m.

where errors up to 60% were found. This is also the location of an error cluster #2 (Fig. 11b). The correlation was 0.8 (Table 6). For most of cross section 6, SfM_A_1m reproduced the measured depth values well (Fig. 10d). However, for depths over 1 m the modelled values had very large errors showing positive values, which also caused the correlation not to be statistically significant (error cluster #3) (Figs. 10d and 11d). Again, the river-bed texture was poorly visible in those areas. Thus, the correlation coefficient was not a reliable indicator of the general performance of the SfM_A_1m in cross section 6. Also the other statistics indicate that the modelled values for areas deeper than 1 m should have been considered as outliers: despite the visually good performance of the SfM_A_1m for depths under 1 m in cross section 6, the ME was −0.44 m and SDE was ±0.71 m (Table 6). The deepest part of cross section 2 was just slightly over 0.6 m and no such error cluster appeared (Fig. 10c). Increasing the resolution from 1 m (SfM_A_1m) to 0.05 m (SfM_A_0.05 m) did not impact the model performance according to the statistics (Table 6), but this is probably because the density of the validation data was not sufficient to capture the scales of variation in topography in the higher resolution model.

Both ADCP_A_1m and Optical_A_1m produced good results for autumn in both cross sections (Fig. 10, Table 6). The correlations for ADCP_A_1m were 0.97 and 0.98 for cross sections 2 and 6, respectively (Table 6). Corresponding values for Optical_A_1m were 0.93 and 0.96. The largest errors of ADCP_A_1m (ADCP) were located in the shallow

areas of cross section 6 (Fig. 10d). Some spatial differences are also noticeable when comparing the statistics of ADCP_A_1m in Tables 4 and 5: the precision was poorer for cross section 6 (SDE = ±0.1 m) compared to cross section 2 (±0.04 m) (Table 6). The spatial extent of the Optical_A_1m was restricted in cross section 6 due to the shadows of the tree canopies (see Fig. 5a and f) and the depth values were under estimated in rest of the section (Fig. 10d). The statistics of Table 6 show that the Optical_A_1m functioned considerably better in cross section 2 compared to cross section 6 in terms of accuracy: the ME for cross section 2 is 0.02 m while in cross section 6 it is −0.14 m. A slight improvement in correlation, ME and SDE appeared from Optical_A_1m to Optical_A_0.05 m, especially in cross section 2.

5. Discussion

Small-scale bathymetric structures, which are geomorphologically important, are often neglected in bathymetric mapping due to the low spatial resolution that traditional survey methods provide. As it was clear that our 1 m resolution models inevitably produce errors when compared with point validation data, 0.05 m models were also produced. The ADCP point density is directly related to the time spent mapping and often the survey time is restricted by changing water level, rapidly changing river bed, daylight, or the limited time of the work force. The resolution of the othoimages that the photogrammetric
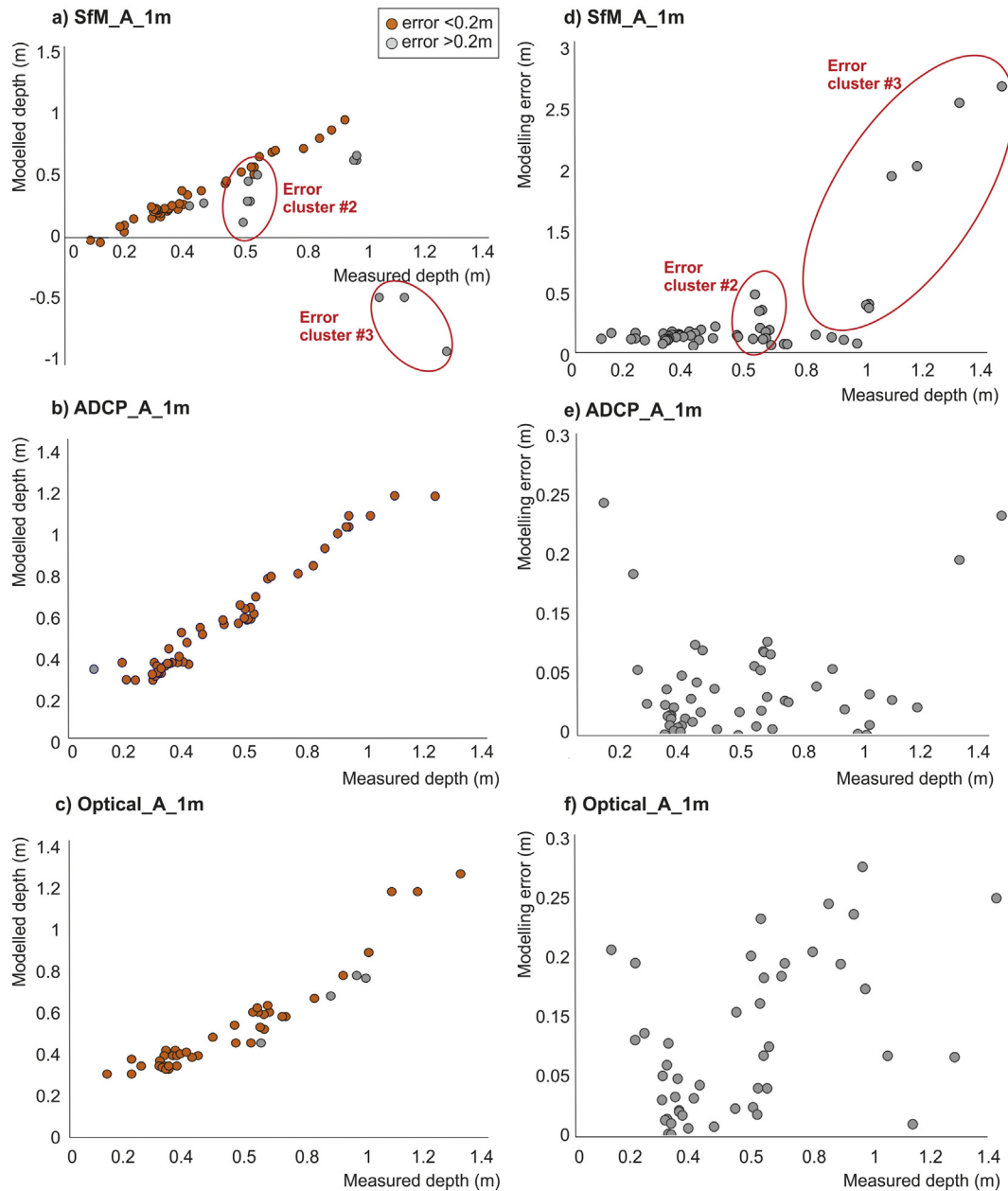
Fig. 9. (a–c) Autumn measured depths plotted against modelled depth for the 1 m resolution models (a) SfM_S_1m, (b) ADCP_S_1m, and (c) Optical_S_1m. The orange plots describe model values that fall within 0.2 m of the validation depth measurements. (d–f) Spring measured depth plotted against the absolute error of the modelled depth value for (d) SfM_S_1m, (e) ADCP_S_1m, and (f) Optical_S_1m.

models were based on was higher than 0.05 m while the ADCP data had notably lower resolution and thus even more interpolation was needed to produce the 0.05 m resolution model of ADCP data. The 0.05 m resolution is more comparable with topographic surveys of non-inundated areas where point densities of a few centimeters are normal (Kasvi et al., 2017a). In our study, the validation data were sparser (point density between 0.3 and 1.3 m) compared to the 0.05 m resolution models.

Table 5
Statistical characteristics describing the quality of the Models 1 and 4 on depths <0.8 m and with all the negative modelled depths removed.

	r	R^2	ME (m)	MAE (m)	Min. error (m)	Max. error (m)	SDE (m)	n
SfM_S_1m	0.71	0.51	0.11	0.21	−0.36	0.71	±0.26	53.00
SfM_A_1m	0.86	0.73	−0.15	0.15	−0.52	−0.05	±0.09	41.00

Therefore, the capability of the models to reproduce the small-scale bathymetric variability was investigated visually.

As the echo sounder was unable to measure depths <0.2 m, the errors of the echo sounding-based models were mostly located in the shallow areas and the spatial extent of the models here was restricted. Nevertheless, the echo sounding produced the most accurate (maximum ME = −0.02 m) and precise (SDE = ±0.08 m or less) models in both spring and autumn. Increasing the model resolution in the autumn from 1 m to 0.05 m required heavier interpolation that, however, did not significantly affect the accuracy (ME) of the ADCP based model (ME changed from −0.01 m to −0.02 m). Our results suggest that the interpolation method used (kriging) functioned well in the study site, which may result from the relatively smooth river bed with only few sudden changes in elevation or cobbles complicating the bed structure. However, as the validation data were also of a low resolution (point density between 0.3 and 1.3 m), it is important to note that how well
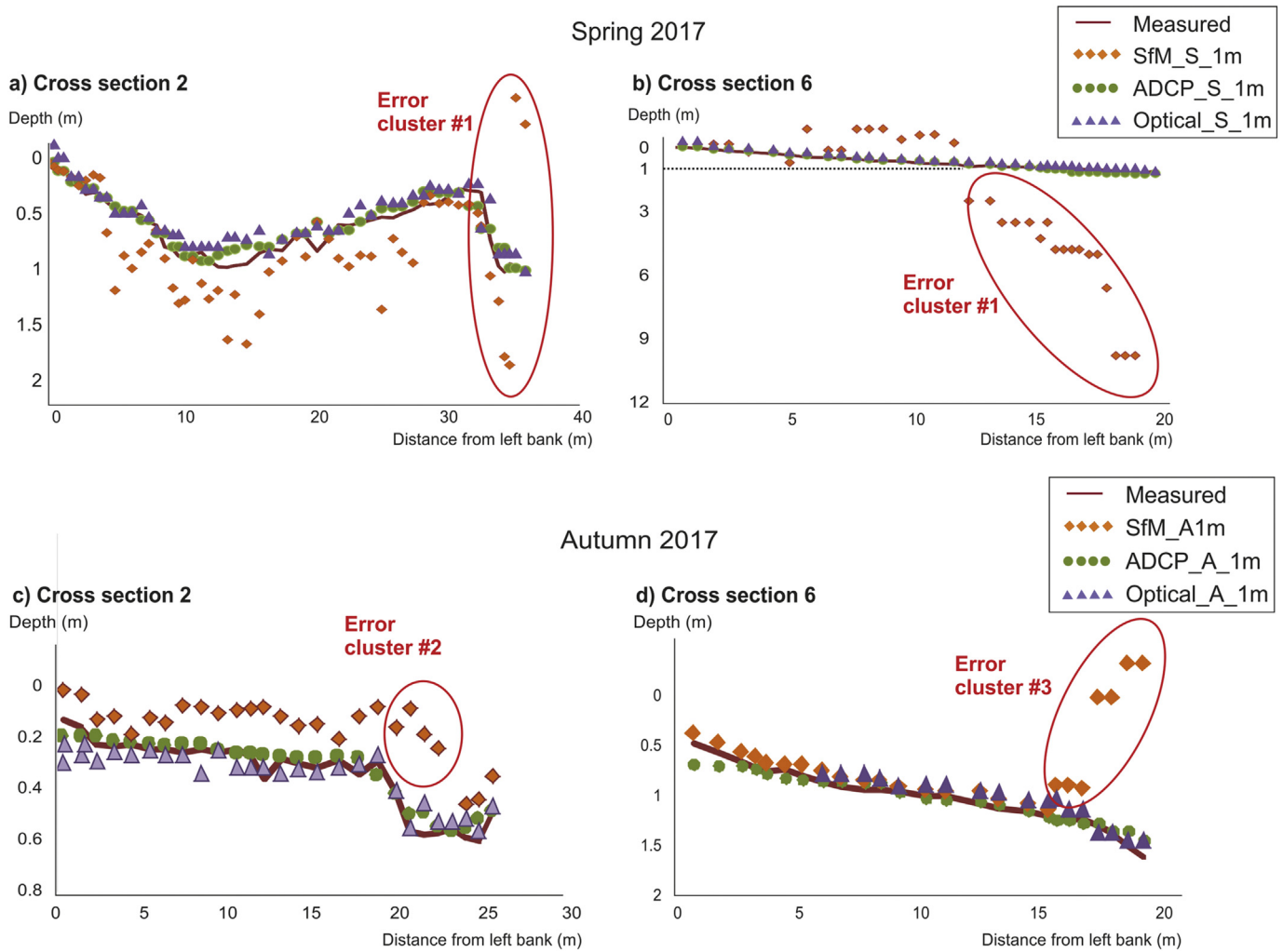
Fig. 10. Validation cross sections 2 and 6 from spring (a and b) and autumn (c and d) for the 1 m resolution models. Note that in autumn, the trees cast shadows on the water surface so that the optical bathymetric model area did not reach the left bank near cross section 6. That is why the optical model validation data points start at 5 m from the shore.

kriging picks up the small-scale bathymetric variability is not revealed in the error statistics. From visual interpretation, these small-scale bed structures, such as ripples, which were clearly visible in the orthomosaics, were not reproduced in the ADCP-based models at all. The low resolution of the data explains, at least partly, the fact that even though the high-flow ADCP data were gathered two days later than the validation data (during which the water level rose 0.2 m), the errors were of the same magnitude compared to the autumn data, indicating that over this period no major bed-level changes have occurred.

In addition to the resolution of the collected dataset and the applied interpolation method, the accuracy and precision of the echo sounding-based model depends also on the accuracy of the depth measurement itself and the quality of the GNSS measurement. In our study, the low-flow ADCP data were georeferenced based on a dGPS instead of a high accuracy VRS-GNSS. Based on our accuracy analysis, the dGPS signal deviates spatially from the mean by a maximum of 0.23 m. Such an error would have implications for data quality, especially for the 0.05 m resolution model. However, our results showed very few differences in the accuracies and precisions between the ADCP-based models using VRS-GNSS and dGPS. Furthermore, achieving a spatially continuous and equally dense dataset would require automatically controlled positioning. Otherwise the point spacing will be random and dependent on the person controlling the device, as in our study. As expected, no association of model accuracy/precision and water color/turbidity in the case of the ADCP was found. It must also be noted that the inability

of ADCP to measure very shallow areas is not visible in the error statistics, as the device does not produce any data on those areas. Further, the density of ADCP sampling was substantially lower than the rate of change of bathymetry evident in aerial images (e.g., Fig. 11b), which is a major disadvantage of the kind of echo sounding used here. Multi-beam echo sounding (MBES) may be a valuable alternative, especially micro-MBES that may work in depths as shallow as 0.50 m (e.g., EdgeTech, 2017). The ADCP device equipped with GPS and remote controlled platform is clearly the most expensive and time consuming of the measurement approaches we used.

Less expensive and less time consuming bathymetric SfM does not require reference measurements from the river bed (Dietrich, 2017). However, for georeferencing the mosaic at high precision, a high quality GNSS is needed, which also benefits from measurement of the wetted perimeter. All in all, our modelling results were poorer compared to Dietrich's (2017) test in a reach of the White River, which had depths across a range comparable to our study (from 0 to ~1.5 m) and bed sediment raging from fine sand to cobbles, similar to the Pulmanki River. According to his study, the approach is capable of producing bathymetric datasets with accuracies of ~0.02% of the flying height and precisions of ~0.1% of the flying height in ideal conditions, which provide a significant improvement in the accuracy and precision for bathymetric SfM datasets compared to Westaway et al. (2003) and Woodget et al. (2015).

In our study both accuracy and precision of the bathymetric SfM improved notably with decreased water color and turbidity in autumn,
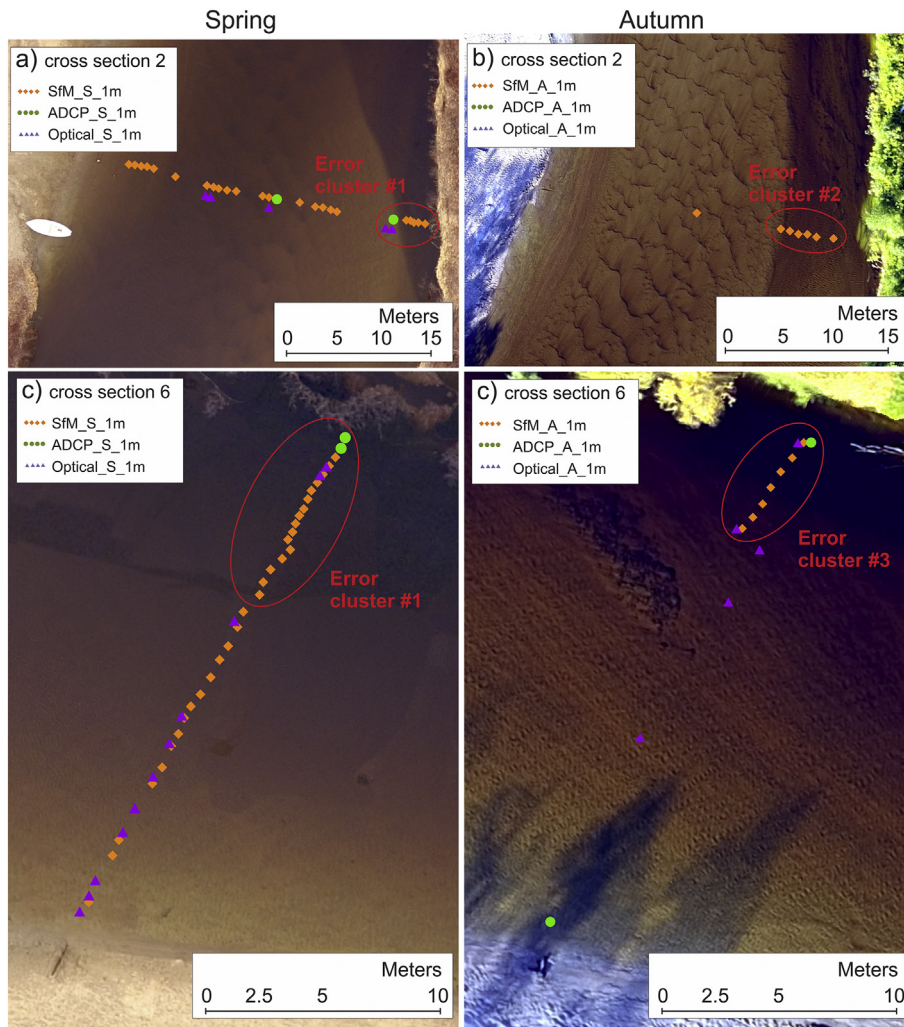
Fig. 11. Over 0.2 m errors of the 1 m resolution models on map. (a) Cross section 2, spring. (b) Cross section 2, autumn. (c) Cross section 6, spring. (d) Cross section 6, autumn.

Table 6
Statistics of the model performance in cross sections 2 and 6. ME = mean error, MAE = mean absolute error, SDE = standard deviation of error. Correlation marked with red color is not statistically significant.

		r	R²	ME (m)	MAE (m)	Min. error (m)	Max. Error (m)	SDE (m)	n
Spring									
SfM_S_1m	CS2	0.58	0.34	0.13	0.27	−1.35	0.72	±0.34	54
	CS6	0.72	0.53	3.20	2.98	−1.45	15.8	±4.03	37
ADCP_S_1m	CS2	0.94	0.89	−0.03	0.06	−0.23	0.29	±0.08	56
	CS6	0.99	0.97	0.00	0.07	−0.18	0.11	±0.07	37
Optical_S_1m	CS2	0.93	0.86	−0.08	0.10	−0.33	0.27	±0.09	56
	CS6	0.99	0.98	−0.17	0.17	−0.34	−0.01	±0.07	37
Autumn									
SfM_A_1m	CS2	0.80	0.63	−0.18	0.18	−0.52	−0.07	±0.09	29
	CS6	−0.33	0.11	−0.44	0.44	−2.41	0.05	±0.71	25
ADCP_A_1m	CS2	0.97	0.93	−0.02	0.03	−0.09	0.07	±0.04	27
	CS6	0.98	0.95	−0.01	0.07	−0.23	0.24	±0.10	25
Optical_A_1m	CS2	0.93	0.87	0.02	0.05	−0.13	0.18	±0.07	29
	CS6	0.96	0.92	−0.14	0.15	−0.26	0.08	±0.08	18
SfM_A_0.05 m	CS2	0.78	0.61	−0.18	0.18	−0.48	−0.04	±0.09	29
	CS6	−0.18	0.03	−0.39	0.39	−3.00	−0.03	±0.76	25
ADCP_A_0.05 m	CS2	0.96	0.93	−0.02	0.03	−0.13	0.07	±0.04	27
	CS6	0.98	0.96	−0.01	0.06	−0.24	0.24	±0.09	25
Optical_A_0.05 m	CS2	0.95	0.89	−0.01	0.05	−0.13	0.09	±0.06	29
	CS6	0.97	0.94	−0.14	0.15	−0.26	0.08	±0.08	18

which is not surprising as this will influence the level of texture recorded on the imagery. During our spring field campaign, the conditions were rather poor for bathymetric SfM even though Secchi depth was not achieved. The relative accuracy of the model was 1.5% of the flying height and the precision was 3.9% of the flying height (calculated for 70 m flying height) (according to James and Robson, 2012). During the more favorable conditions in September, the relative accuracy was 0.4% of the flying height and the precision was 0.7% of the flying height, still not as good as the results reported in Dietrich (2017).

The sources of error in bathymetric SfM include georeferencing errors, noise in the point cloud (originating from the SfM process) and water surface elevation errors (Dietrich, 2017). The SfM reconstruction process itself may cause random noise, especially in areas with low texture (Fonstad et al., 2013). The light wave is also affected by the water turbidity and color. In spring, higher accuracy and precision were achieved in cross section 2 (ME = 0.13 m, SDE = ±0.34 m) compared to cross section 6 (ME = 3.2 m, SDE = ±4.03 m). Visual interpretation suggests that the river bed in cross section 2 has more texture (ripples) that might have enhanced the SfM procedure. In general, the bed profile in our study site was relatively smooth. Dietrich (2017) also found that the modelling error was at some locations associated with areas in the original SfM point cloud with higher roughness. However, he did not find this to be associated with under-prediction of the depth or even existence of river bedforms. The quality of the bathymetric SfM was also clearly dependent on depth; errors increased in areas with depths

of >0.8 m. Removing areas deeper than 0.8 m and the negative modelled depths diminished the ME from 1.37 m to 0.11 m, and the SDE from ±2.88 m to ±0.26 m in spring. This may have been a consequence of exceeding the maximum detectable depth, i.e., the river bed was not visible for the camera anymore or the river bed texture was lost at greater depths with high turbidity. The results of Dietrich (2017) did not show such a clear error-depth dependence. However, we deduced that even though the turbidity or color was not mentioned in his study, it is probable that those values were higher during our survey compared to his. This would explain the poorer performance of the SfM model, especially on spring, as the river bed texture was poorly visible in areas with large errors. Thus, the conditions at the study site cannot be considered as "ideal".

Further, our statistical and visual investigation suggested that the errors in SfM models were rather systematic in nature and the modelled depths were either positively or negatively biased, which is typical for photogrammetric approaches (e.g., Westaway et al., 2001). In spring, the depth values were mostly over-estimated and in autumn under-estimated. This also suggests that the prevailing circumstances, such as the water color, turbidity, light and bed material affect the modelling results and taking these factors into account could enhance the model performance. Shintani and Fonstad (2017) used bathymetric SfM with a site specific refraction index instead of the constant fresh water refraction index (1.337). They calculated the site specific index by deriving a linear regression between in situ depth measurements and the modelled depth values. In their study, the site specific correction approach provided the best results (compared to constant refraction index and optical modelling approaches) even though the method also had systematic error. They also removed more modelled points by manual filtering: they excluded areas with extreme shadow, white water, low photograph overlap or 'negative actual depths'. In our study, we used automatic filtering, which apparently did not remove the low quality data points well enough, but on the other hand it was objective and consistent. Finally, the effectiveness of the bathymetric correction is strongly sensitive to modelling of the water surface and this may lead to the kind of systematic error recorded here.

By contrast, Shintani and Fonstad (2017) found that optical modelling did not produce good results from their study site, which contains local variations in substrate colors, surface turbulence and large amounts of shadow between cobbles and gravels, all leading to varying reflectance values independent on depth. It is well known that the main disadvantages of optical modelling are related to water turbidity, shadows, varying light conditions during the measurements, and heterogeneous river bed material (Flener, 2013; Tamminga et al., 2014; Williams et al., 2014). In this study, we removed the areas shadowed by tree canopies in order to avoid these errors. These areas were located close to shorelines and restricted the model coverage to some degree. Based on our experience, low sun angles limit the usage of optical modelling especially in high latitude environments, and the modelling should be performed close to midday, if possible, in other latitudes as well. Furthermore, sun glint may cause errors, which were not present in our data (e.g., Overstreet and Legleiter, 2017). Correlations between the measured and modelled depth values were 0.96 both in spring and autumn. The autumn models (ME = −0.05) were more accurate compared to the spring model (ME = −0.12), suggesting that the turbidity and color have disturbed model performance in spring. Compared to the ADCP, the optical model produced very similar correlations and precisions in both spring and autumn. However, a visual investigation showed that the small-scale bedforms were clearly better described by the 0.05 m optical models compared to 0.05 m ADCP model. This is an important result, as the validation data were not dense enough to enable these properties to be present in error statistics.

Optical modelling produced some systematic errors with no clear association with depth or site-specific factors. The optical models errors were 0.14% of the flying height in spring and 0.07% in autumn, of the same order of magnitude as those of Flener et al. (2013), who used

Lyzenga's model on the same river reach to model the bathymetry at 0.05 m resolution. Their models relative accuracies were approximately between 0.1 and 0.17% of the flying height. Based on our results and the comparisons with previous studies it seems that optical modelling provides a feasible and cost-efficient approach for high resolution bathymetric modelling of shallow water, but it requires a smooth river bed with no surface turbulence, cobbles and gravels. The errors in optical bathymetric values, caused by river bed substrate variability, was not a problem in our study area. However, they may be overcome by using a band-ratio instead of a single-band approach (e.g., Legleiter et al., 2004; Williams et al., 2014). Tests in this study did not find support for such a conclusion. On the other hand, optical modelling is not as sensitive to water color and turbidity as the bathymetric SfM approach.

6. Conclusions

Bathymetry is one of the most important measurable features when studying underwater river environments. In this study we have tested three promising remote sensing methods to survey shallow water bathymetry with high resolution. Remote sensing techniques are favorable for bathymetric mapping as they don't disturb the water body or the river bed and are rather rapid to execute. We modelled a 500 m reach (only 100 m reach with ADCP) of a meandering river, ~30 m in width, during a rising spring flood (Q = 10–15 m³/s) with high color, and during autumn low discharge (Q = 4 m³/s) with low turbidity and color. We applied echo sounding and two photogrammetry-based methods: bathymetric SfM and optical modelling. In spring we created a 1 m resolution model, and in autumn both 1 m and 0.05 m resolution models. We compared the resultant nine bathymetric models with 93 and 54 measured points with depths between 0 m and 1.5 m in the spring and autumn, respectively. The following conclusions can be made.

First, ADCP-based echo sounding provided the most accurate (ME ~ −0.02 m) and precise (SDE < ±0.08 m) bathymetric models when compared to validation data with an average point spacing of 0.86 m. The modelled values correlated well (r = ~0.97) with the validation points. The modelling errors varied between −0.25 m and +0.25 m. Flow turbidity, color or depth, riparian vegetation and weather conditions did not affect the measurements. Our study site has a relatively smooth river bed with only~ few sudden changes in bathymetry and no stones and cobbles, which probably enabled a successful interpolation of the ADCP measurements with point density of 0.63–1.3 points/m². However, the high-level interpolation, which was required to create the 0.05 m resolution ADCP model, was not able to reproduce the small-scale bathymetric variability that was visually evident in the orthomosaics. Our validation data were probably not dense enough to reproduce those bedforms and thus this issue was not detectable in our error statistics, only visually appreciable. The quality of an ADCP-based high-resolution bathymetric model is highly dependent on the selected interpolation method. The main limitations of ADCP are its low spatial resolution, inability to measure depths <0.2 m (which also severely limited the spatial extent of our surveys), and its labor-intensiveness. Thus, ADCP is not suitable for mapping large areas or areas with large proportion of very shallow water in high resolution. It should not be applied when small-scale bedforms are of interest. It is also by far the most expensive of the approaches that we tested.

Second, the quality of the bathymetric SfM was highly sensitive to flow turbidity and color: ME declined from 1.37 m to −0.3 m, and SDE from ±2.88 m to ±0.5 m from spring to autumn, respectively. Due to the turbidity, the quality of the model was clearly dependent on depth; errors increased notably in areas with depths >0.8 m and in areas where the bed structure was not clearly visible. Removing areas deeper than 0.8 m and the negative modelled depths diminished the ME from 1.37 m to 0.11 m, and the SDE from ±2.88 m to ±0.26 m in spring. Our results and the literature review indicate that the bathymetric SfM requires, in addition to clear water, a clearly visible bed

with enough structure, as shown to be crucial in classical photogrammetric mapping of stream bathymetry (Lane et al., 2010). It is possible that the smooth sandy bed in our study site did not provide enough structure for the SfM process to work properly, especially when visibility was poor. On the other hand, bathymetric SfM does not suffer as much as optical modelling from substrate variability, turbulent flow or large stones and cobbles on the river bed. The effect of depth, color and turbidity, and other site specific factors on the bathymetric SfM needs further research.

Third, our study area was suitable for optical modelling: substrate color was consistent, the river bed was smooth with no large stones and cobbles and the flow was not turbulent. In many ecologically important areas such as floodplains with high vegetation density or fish spawning areas with turbulent flow and bed structure, optical modelling would suffer from reflectance variation that does not depend on the depth. Color and depth did affect the optical models functionality to some extent, but clearly less than the bathymetric SfM. The errors were 0.14% of the flying height in spring and 0.07% in autumn. Model accuracy improved in autumn with lower water color and turbidity (ME = −0.05 m) compared to spring (ME = −0.12 m). Correlations between the measured and modelled depth values ($r = 0.96$) and the model's precision (SDE = ±0.09–0.11 m) were close to those achieved with echo sounding. Shadows caused by riparian vegetation restricted the spatial extent of the optical models.

While techniques to measure and model bathymetry have improved continuously, there is still no approach that allows ready mapping of shallow water areas with high accuracy, precision and resolution. However, a sophisticated choice of the approach taking into account site-specific characteristics will improve the results. In many cases, a combination of several methods should provide the most feasible survey approach.

Acknowledgements

References

Brasington, J., Rumsby, B.T., McVey, R.A., 2000. Monitoring and modelling morphological change in a braided gravel-bed river using high resolution GPS-based survey. Earth Surf. Process. Landf. 25, 973–990. https://doi.org/10.1002/1096-9837(200008)25:9<973::AID-ESP111>3.0.CO;2-Y.

Carbonneau, P.E., Dietrich, J.T., 2017. Cost-effective non-metric photogrammetry from consumer-grade sUAS: implications for direct georeferencing of structure from motion photogrammetry. Earth Surf. Process. Landf. 42, 473–486. https://doi.org/10.1002/esp.4012.

Carbonneau, P.E., Lane, S.N., Bergeron, N., 2006. Feature based image processing methods applied to bathymetric measurements from airborne remote sensing in fluvial environments. Earth Surf. Process. Landf. 31, 1413–1423. https://doi.org/10.1002/esp.1341.

Dierssen, H.M., Zimmerman, R.C., Leathers, R.A., Downes, T.V., Davis, C.O., 2003. Ocean color remote sensing of seagrass and bathymetry in the Bahamas Banks by high-resolution airborne imagery. Limnol. Oceanogr. 48, 444–455. https://doi.org/10.4319/lo.2003.48.1_part_2.0444.

Dietrich, J.T., 2017. Bathymetric Structure-from-Motion: extracting shallow stream bathymetry from multi-view stereo photogrammetry. Earth Surf. Process. Landf. 42, 355–364.

DJI, 2019. DJI's smartest flying camera ever. [WWW Document]. DJI Official. URL https://www.dji.com/fi/phantom-4 (accessed 3.4.19).

Dost, R.J.J., Mannaerts, C.M., 2008. Generation of lake bathymetry using sonar, satellite imagery and GIS. In: Dangermond, J. (Ed.), Proceedings of the 2008 ESRI International User Conference: GIS, Geography in Action. Faculty of Geo-Information Science and Earth Observation, Water Resources, San Diego, Florida.

EdgeTech, 2017. 6205 bathymetry & side scan system - user hardware manual [WWW document]. https://www.edgetech.com/wp-content/uploads/2015/07/0014877_REV_E.pdf, Accessed date: 12 January 2019.

Flener, C., 2013. Estimating deep water radiance in shallow water: adapting optical bathymetry modelling to shallow river environments. Boreal Environ. Res. 18, 488–502.

Flener, C., Vaaja, M., Jaakkola, A., Krooks, A., Kaartinen, H., Kukko, A., Kasvi, E., Hyyppä, H., Hyyppä, J., Alho, P., 2013. Seamless mapping of river channels at high resolution using mobile LiDAR and UAV-Photography. Remote Sens. 5, 6382–6407.

Flener, C., Wang, Y., Laamanen, L., Kasvi, E., Vesakoski, J.-M., Alho, P., 2015. Empirical modeling of spatial 3D flow characteristics using a remote-controlled ADCP System: monitoring a spring flood. Water 7, 217–247. https://doi.org/10.3390/w7010217.

Fonstad, M.A., Dietrich, J.T., Courville, B.T., Jensen, J.L., Carbonneau, P.E., 2013. Topographic structure from motion: a new development in photogrammetric measurement. Earth Surf. Process. Landf. 38, 421–430.

Gilvear, D.J., Waters, T.M., Milner, A.M., 1995. Image analysis of aerial photography to quantify changes in channel morphology and instream habitat following placer mining in interior Alaska. Freshw. Biol. 34, 389–398. https://doi.org/10.1111/j.1365-2427.1995.tb00897.x.

Guenther, G.C., 2007. Airborne Lidar bathymetry. In: Maune, D. (Ed.), Digital Elevation Model Technologies and Applications: the DEM Users Manual, Second edition American Society for Photogrammetry and Remote Sensing, Bethesda, Maryland, pp. 253–329.

Guerrero, M., Lamberti, A., 2011. Flow field and morphology mapping using ADCP and multibeam techniques: survey in the Po River. J. Hydraul. Eng. 137, 1576–1587. https://doi.org/10.1061/(ASCE)HY.1943-7900.0000464.

Harvey, A.H., Gallagher, J.S., Sengers, J.M.H.L., 1998. Revised formulation for the refractive index of water and steam as a function of wavelength, temperature and density. J. Phys. Chem. Ref. Data 27, 761. https://doi.org/10.1063/1.556029.

Hillade, R.C., Raff, D., 2008. Assessing the ability of airborne LiDAR to map river bathymetry. Earth Surf. Process. Landf. 33, 773–783.

James, M.R., Robson, S., 2012. Straightforward reconstruction of 3D surfaces and topography with a camera: accuracy and geoscience application. J. Geophys. Res. Earth Surf. 117.

James, M.R., Robson, S., 2014. Mitigating systematic error in topographic models derived from UAV and ground-based image networks. Earth Surf. Process. Landf. 39, 1413–1420.

Javernick, L., Brasington, J., Caruso, B., 2014. Modeling the topography of shallow braided rivers using Structure-from-Motion photogrammetry. Geomorphology 213, 166–182.

Kaeser, A.J., Litts, T.L., Tracy, T.W., 2013. Using low-cost side-scan sonar for benthic mapping throughout the lower Flint River, Georgia, USA: low-cost sonar benthic mapping in rivers. River Res. Appl. 29, 634–644. https://doi.org/10.1002/rra.2556.

Kasvi, E., Vaaja, M., Alho, P., Hyyppä, H., Hyyppä, J., Kaartinen, H., Kukko, A., 2013. Morphological changes on meander point bars associated with flow structure at different discharges. Earth Surf. Process. Landf. 38, 577–590. https://doi.org/10.1002/esp.3303.

Kasvi, E., Hooke, J.M., Kurkela, M., Vaaja, M., Virtanen, J.-P., Hyyppä, H., Hyyppä, J., 2017a. Modern empirical and modelling study approaches in fluvial geomorphology to elucidate sub-bend-scale meander dynamics. Prog. Phys. Geogr. 41, 533–569.

Kasvi, E., Laamanen, L., Lotsari, E., Alho, P., 2017b. Flow patterns and morphological changes in a sandy meander bend during a flood - spatially and temporally intensive ADCP measurement approach. Water 9, 106.

Kinzel, P.J., Wright, C.W., Nelson, J.M., Burman, A.R., 2007. Evaluation of an experimental LiDAR for surveying a shallow, braided, sand-bedded river. J. Hydraul. Eng. 133, 838–842.

Kinzel, P.J., Legleiter, C.J., Nelson, J.M., 2013. Mapping river bathymetry with a small footprint green LiDAR: applications and challenges. J. Am. Water Resour. Assoc. 49, 183–204.

Koljonen, S., Huusko, A., Mäki-Petäys, A., Louhi, P., Muotka, T., 2012. Assessing habitat suitability for juvenile Atlantic salmon in relation to in-stream restoration and discharge variability. Restor. Ecol. 21, 344–352.

Lane, S.N., Richards, K.S., Chandler, J.H., 1994. Developments in monitoring and modelling small-scale river bed topography. Earth Surf. Process. Landf. 19, 349–368. https://doi.org/10.1002/esp.3290190406.

Lane, S.N., Widdison, P.E., Thomas, R.E., Ashworth, P.J., Best, J.L., Lunt, I.A., Smith, G.H.S., Simpson, C.J., 2010. Quantification of braided river channel change using archival digital image analysis. Earth Surf. Process. Landf. 35, 971–985. https://doi.org/10.1002/esp.2015.

Legleiter, C.J., 2016. Inferring river bathymetry via Image-to-Depth Quantile Transformation (IDQT). Water Resour. Res. 52, 3722–3741. https://doi.org/10.1002/2016WR018730.

Legleiter, C.J., Robetrs, D.A., Marcus, W.A., Fonstad, M.A., 2004. Passive optical remote sensing of river channel morphology and in-stream habitat: physical basis and feasibility. Remote Sens. Environ. 93, 493–510.

Lyzenga, D.R., 1981. Remote sensing of bottom radiance and water attenuation parameters in shallow water using air-craft and Landsat data. Int. J. Remote Sens. 2, 71–82.

Mandlburger, G., Pfennigbauer, M., Wieser, M., Riegl, U., Pfeifer, N., 2016. Evaluation of a novel UAV-borne topo-bathymetric laser profiler. ISPRS - International Archives of the Photogrammetry, Remote Sensing and Spatial Information Sciences XLI-B1, pp. 933–939 https://doi.org/10.5194/isprsarchives-XLI-B1-933-2016.

Marcus, W.A., Fonstad, M.A., 2008. Optical remote mapping of rivers at sub-meter resolutions and watershed extents. Earth Surf. Process. Landf. 33, 4–24. https://doi.org/10.1002/esp.1637.

McKean, J., Nagel, D., Tonina, D., Bailey, P., Wright, C.W., Bohn, C., Nayegandhi, A., 2009. Remote sensing of channels and riparian zones with a narrow-beam aquatic-terrestrial LIDAR. Remote Sens. 1. https://doi.org/10.3390/rs1041065.

Micheletti, N., Chandler, J.H., Lane, S., 2015a. Structure from motion (SFM) photogrammetry. In: Clarke, L.E., Nield, J.M. (Eds.), Geomorphological Techniques. British Society for Geomorphology, London, UK.

Micheletti, N., Lane, S.N., Chandler, J.H., 2015b. Application of archival aerial photogrammetry to quantify climate forcing of alpine landscapes. Photogramm. Rec. 30, 143–165. https://doi.org/10.1111/phor.12099.

Milne, J.A., Sear, D.A., 1997. Modelling river channel topography using GIS. Int. J. Geogr. Inf. Sci. 11, 499–519.

Overstreet, B.T., Legleiter, C.J., 2017. Removing sun glint from optical remote sensing images of shallow rivers. Earth Surf. Process. Landf. 42, 318–333. https://doi.org/10.1002/esp.4063.

Powers, J., Brewer, S.K., Long, J.M., Campbell, T., 2015. Evaluating the use of side-scan sonar for detecting freshwater mussel beds in turbid river environments. Hydrobiology 743, 127–137.

RIEGL, 2018. UAV-based surveying system for hydrographic applications [WWW document]. http://www.riegl.com/products/unmanned-scanning/bathycopter/, Accessed date: 11 January 2019.

Shintani, C., Fonstad, M.A., 2017. Comparing remote-sensing techniques collecting bathymetric data from a gravel-bed river. Int. J. Remote Sens. 38, 2883–2902.

Sontek, 2016. Sontek riversurveyor M9 [WWW document]. http://www.sontek.com/productsdetail.php?RiverSurveyor-S5-M9-14.

Stumpf, R.P., Holderied, K., Sinclair, M., 2003. Determination of water depth with high-resolution satellite imagery over variable bottom types. Limnol. Oceanogr. 48, 547–556. https://doi.org/10.4319/lo.2003.48.1_part_2.0547.

Tamminga, A., Hugenholtz, C.H., Eaton, C.H., Laponite, M., 2014. Hydrogeomorphology-ecology interactions in river systems. River Res. Appl. 31, 379–391.

Tamminga, A., Hugenholtz, C., Eaton, B., Laponite, M., 2015. Hyperspatial remote sensing of channel reach morphology and hydraulic fish habitat using an unmanned aerial vehicle (UAV): a first assessment in the context of river research and management. River Res. Appl. 31, 379–391. https://doi.org/10.1002/rra.2743.

Tonina, D., McKean, J.A., Benjankar, R.M., Wright, C.W., Goode, J.R., Chen, Q., Reeder, W.J., Carmichael, R.A., Edmondson, M.R., 2018. Mapping river bathymetries: evaluating topobathymetric LiDAR survey. Earth Surf. Process. Landf. https://doi.org/10.1002/esp.4513.

Westaway, R.M., Lane, S.N., Hicks, D.M., 2000. The development of an automated correction procedure for digital photogrammetry for the study of wide, shallow, gravel-bed rivers. Earth Surf. Process. Landf. 25, 209–226. https://doi.org/10.1002/(SICI)1096-9837(200002)25:2<209::AID-ESP84>3.0.CO;2-Z.

Westaway, R.M., Lane, S.N., Hicks, D.M., 2001. Remote sensing of clearwater, shallow, gravel-bed rivers using digital photogrammetry. Photogramm. Eng. Remote. Sens. 67, 1271–1282.

Westaway, R.M., Lane, S.N., Hicks, D.M., 2003. Remote survey of large-scale braided, gravel-bed rivers using digital photogrammetry and image analysis. Int. J. Remote Sens. 24, 795–815. https://doi.org/10.1080/01431160110113070.

Westoby, M.J., Brasington, J., Glasser, N.F., Hambrey, M.J., Reynolds, J.M., 2012. 'Structure-from-Motion' photogrammetry: a low-cost, effective tool for geoscience applications. Geomorphology 179, 300–314. https://doi.org/10.1016/j.geomorph.2012.08.021.

Williams, R.D., Brasington, J., Vericat, D., Hicks, D.M., 2014. Hyperscale terrain modelling of braided rivers: fusing mobile terrestrial laser scanning and optical bathymetric mapping: hyperscale terrain modelling of braided rivers. Earth Surf. Process. Landf. 39, 167–183. https://doi.org/10.1002/esp.3437.

Winterbottom, S.J., Gilvear, D.J., 1997. Quantification of channel bed morphology in gravel-bed rivers using airborne multispectral imagery and aerial photography. Regul. Rivers Res. Manag. 13, 489–499.

Woodget, A.S., Carbonneau, P.E., Visser, F., Maddock, I.P., 2015. Quantifying submerged fluvial topography using hyperspatial resolution UAS imagery and structure from motion photogrammetry. Earth Surf. Process. Landf. 47–64.

Wright, C.W., Kranenburg, C.J., Troche, R.J., Mitchell, R.W., Nagle, D.B., 2016. Depth Calibration of the Experimental Advanced Airborne Research Lidar, EAARL-B (Report No. 2016–1048), Open-File Report. (Reston, VA). https://doi.org/10.3133/ofr20161048.

Yorke, T.H., Oberg, K.A., 2002. Measuring river velocity and discharge with acoustic Doppler profilers. Flow Meas. Instrum. 13, 191–195.

YSI Inc., 2010. YSI 9300 and 9500 Photometers. User Manual (Yellow Springs, Ohio, USA).